國立臺灣大學理學院化學所

碩士論文

Department of Chemistry

College of Science

National Taiwan University

Master’s Thesis

以分子動力學模擬極紫外光微影的化學放大光阻

Exploring Polymer Architecture and PAG Behavior in EUV Chemically Amplified Resists Using MD Simulations

毛威凱

Wei-Kai Mao

指導教授: 鄭原忠 博士

Advisor: Yuan-Chung Cheng Ph.D.

中華民國 113 年 11 月

November, 2024

doi:10.6342/NTU202404559

Acknowledgements

我衷心感謝我的指導教授鄭原忠博士，感謝他在我的研究過程中耐心地給予我指導和支持。他在分子模擬方面的專業知識與見解對我的論文至關重要。我也要特別感謝我的實驗室同儕，在困難的時刻給予我學習上的幫助和情感上的支持。

最後，我要感謝我的家人，因為他們始終如一的鼓勵，還有我的朋友們，在我需要放鬆的時候總是陪伴在我身邊。沒有你們的支持，這篇論文是無法完成的。

摘要

這篇論文透過分子動力學 (MD) 模擬研究了用於極紫外光 (EUV) 微影技術的化學增幅光阻 (CAR) 中聚合物架構與光致產酸劑 (PAG) 分佈的行為。通過對四種不同的 CAR 系統進行建模（包括自由和鍵合陰離子類型），本研究探討了不同聚合物結構如何影響化學分佈的均勻性。通過對徑向分佈函數 (RDF)、數密度分佈和離子的空間分群的分析，其結果顯示鍵合陰離子能夠減少陰離子和陽離子的聚集，從而提高技術的穩定性。此外，對聚合物剛性和可動性的研究表明，較剛性的聚合物單元會限制整個系統的可動性。這些發現為優化下一代半導體製造中的 CAR 配方提供了重要的見解，特別是在圖形解析度的方面。

關鍵字：分子動力學、化學增強光阻、極紫外光微影、聚合物結構、光致產酸劑、離子空間分群

doi:10.6342/NTU202404559

Abstract

This thesis investigates the behavior of polymer architecture and PAG distribution in CARs for EUV photolithography through MD simulations. By modeling four distinct CAR systems, including free and bonded-anion types, this study explores how different polymer structures influence the uniformity of chemical distribution. Through the analysis of RDFs, number density distributions, and ion clustering behavior, the results show that bonded anions reduce aggregation in both anions and cations, enhancing material stability. Additionally, studies of polymer rigidity and mobility reveal that more rigid polymer units limit the mobility of overall system. These findings offer critical insights into the optimization of CAR formulations for next-generation semiconductor manufacturing, especially in feature resolution and pattern fidelity.

Keywords: Molecular Dynamics, Chemically Amplified Resist, EUV Lithography, Polymer Architecture, Photoacid Generator, Ion Clustering

doi:10.6342/NTU202404559

Contents

doi:10.6342/NTU202404559

doi:10.6342/NTU202404559

doi:10.6342/NTU202404559

List of Figures

doi:10.6342/NTU202404559

List of Tables

doi:10.6342/NTU202404559

Denotation

IC	積體電路 (Integrated Circuits)
UV	紫外光 (ultraviolet light)
PR	光阻 (photoresist)
PEB	曝光後烘烤 (post-exposure bake)
DNQ	重氮萘醌 (diazonaphthoquinone)
CAR	化學增幅光阻 (chemically amplified resist)
PAG	光致產酸劑 (photoacid generator)
DUV	深紫外光 (deep ultraviolet)
EUV	極紫外光 (extreme ultraviolet)
LER	邊緣粗糙度 (line-edge roughness)
LWR	線寬粗糙度 (line-width roughness)
TPS	三苯基鋶 (triphenylsulfonium)

TFL	三氟甲磺酸根 (triflic anion)
MD	分子動力學 (molecular dynamics)
PBC	週期性邊界條件 (periodic boundary condition)
PME	粒子網格埃瓦爾德法 (particle mesh Ewald)
FFT	快速傅立葉轉換 (fast Fourier transforms)
MSD	平均平方位移 (mean square displacement)
RDF	徑向分佈函數 (radial distribution function)
LCST	低臨界溶解溫度 (lower critical solution temperature)
Tg	玻璃轉化溫度 (glass transition temperature)

doi:10.6342/NTU202404559

Chapter 1 Introduction

1.1 Semiconductor Photolithography

Semiconductor photolithography is the cornerstone of modern semiconductor manufactory, enabling the creation of complex microelectronic circuits that are essential for a wide range of applications, from consumer electronics to advanced computing systems. Photolithography involves the transfer of complex circuit patterns from a photomask onto the surface of a semiconductor wafer, typically made of silicon. The successful execution of this process is critical for defining the structures that form transistors and memory cells, which are the fundamental building blocks of integrated circuits (ICs).

In recent decades, the demand for higher performance and greater efficiency in electronic devices has driven the semiconductor industry to continually shrink the feature sizes of these circuits. The transition from micron-scale to nanoscale structures has brought about challenges in photolithography, requiring more precise control over each step of the process. A key step in photolithography is the application of a photoresist (PR), a light-sensitive material that responds to ultraviolet (UV) light exposure. After coated onto the wafer, the photoresist is exposed to light through a photomask, which defines the circuit pattern. After a heating process named post eaxposure bake (PEB), the exposed areas of the photoresist undergo chemical changes that allow selective removal during the development stage, revealing the desired pattern on the wafer.

The next stage involves the etching of the wafer surface, where the areas not protected by the remaining photoresist are removed to create the physical structures for circuit functionality. Throughout this multi-step process, the resolution and sensitivity of the photoresist are critical factors that determine the overall performance and yield of the semiconductor devices. With the ongoing push toward sub-10 nm feature sizes, these requirements have become even more difficult, leading to the development of new materials and techniques in photolithography.

1.1.1 Functions of photoresists

The role of photoresists in photolithography is to enable the precise transfer of circuit patterns onto the semiconductor substrate. This is achieved by the ability of photoresist to change its chemical properties when exposed to light. Depending on the nature of the photoresist, the exposure either increases or decreases the material’s solubility in a developer solution, thereby allowing selective removal of either the exposed or unexposed regions. Based on the regions of removal, photoresists can be classified into two categories: positive and negative resists.

In a positive photoresist, the regions exposed to light become more soluble in the developer solution, allowing the exposed areas to be washed away during development. This results in a pattern that corresponds to the photomask, where the unexposed areas remain intact. Positive resists are widely used in semiconductor manufacturing due to their high resolution and ability to produce finer features. Conversely, in a negative photoresist, the regions exposed to light become less soluble, meaning that the unexposed areas are

doi:10.6342/NTU202404559

removed during development, leaving the exposed regions to define the pattern. Positive photoresists have played a important role in the evolution of semiconductor manufacturing, particularly in the context of shrinking device sizes and increasing complexity.

One of the earliest positive photoresists was developed using a combination of Novolac resin and diazonaphthoquinone (DNQ) as the photosensitive component, known as AZ photoresists, which were marketed in the 1970s. This marked a significant milestone as positive photoresists gained recognition for their superior resist contrast, ultimately replacing all negative photoresists then in high-end photolithography applications. This advancement enabled the precise transfer of complex patterns onto semiconductor substrates, a critical improvement for the production of integrated circuits during the rapid expansion of the microelectronics industry.

Positive resists gained further prominence in the 1980s with the development of chemically amplified resists (CARs), a breakthrough technology that significantly improved sensitivity and resolution. CARs relied on photoacid generators (PAGs) that released acid upon UV exposure, triggering a catalytic reaction that amplified the changes in solubility, even with minimal light exposure. This technology proved essential for advanced lithographic processes[1, 2]. As deep ultraviolet (DUV) lithography, using a wavelength of 193 nm, became the industry standard in the late 20th century, positive resists continued to evolve. However, the challenges presented by extreme ultraviolet (EUV) lithography, with its shorter 13.5 nm wavelength, required further advancement in photoresist chemistry[3]. Researchers focused on improving the absorbance and sensitivity of positive resists, addressing issues like acid diffusion and line-edge roughness (LER). Despite these challenges, positive photoresists have remained essential materials in photolithography, playing a significant role in the ongoing advancement of semiconductor

doi:10.6342/NTU202404559

technologies. It is believed that with precise control over the atomic structure, positive photoresists can continue to make progress, enhancing film homogeneity and pattern resolution[2].

1.1.2 Overview of chemically amplified resist

Chemically amplified resists (CARs) have transformed the landscape of photolithography, particularly in the domains of deep ultraviolet (DUV) and extreme ultraviolet (EUV) lithography. CARs differ from traditional photoresists in that they utilize a catalytic reaction to amplify the chemical changes initiated by light exposure. While traditional photoresists undergo a single change for each photon, CARs can produce multiple changes from a single photon. In a typical CAR system, the resist consists of a polymer matrix embedded with photoacid generators (PAGs). The polymer matrix often contains a significant amount of sensitizer, which enhances UV absorbance, as well as protecting groups that modulate the chemical properties of the resist.

Upon exposure to UV light, primary electrons are ejected from atoms within the polymer matrix. These primary electrons scatter and generate secondary electrons, which further interact with the material. When these secondary electrons encounter the PAG molecules, such as triphenylsulfonium (TPS), they generate acids. The acids act as catalysts, triggering the removal of the protecting groups in the polymer. This process alters the polarity of the resist, making the exposed regions more soluble to water, allowing for selective removal during the development stage[4]. The amplification mechanism inherent in CARs enables a significantly higher sensitivity compared to conventional resists, as a single photon can initiate multiple catalytic reactions. This leads to a huge increase in solubility in the exposed areas, facilitating finer feature patterning. However, the high sensitivity of CARs introduces other challenges, particularly in controlling line edge roughness (LER) and line width roughness (LWR)[5]. To prevent excessive diffusion of the photoacid, which can lead to pattern loss, the distribution of the generated acids within the resist must be carefully controlled. Despite these challenges, CARs remain a great choice of material for advanced lithography due to their superior resolution, sensitivity, and ability to produce patterns with sub-50 nm feature sizes.

1.2 Chemically Amplified Resist in EUV Photolithography

Extreme ultraviolet (EUV) photolithography represents the latest advancement in the pursuit of smaller feature sizes in semiconductor manufacturing. Operating at a wavelength of 13.5 nm, EUV offers significantly finer resolution compared to previous generations of lithography, such as deep ultraviolet (DUV) at 193 nm. The adoption of EUV technology has been a critical step in enabling the fabrication of chips with feature sizes below 10 nm, which are essential for the continued scaling of semiconductor devices in accordance with Moore’s Law.

Chemically amplified resists (CARs) have been adapted for EUV lithography, optimizing their performance under the unique and demanding conditions of this technology. Developing CARs suitable for EUV requires new formulations that incorporate advanced photoacid generators (PAGs) and polymer architectures, designed to minimize acid diffusion and enhance pattern fidelity. To achieve these goals, research teams have reformulated CAR components to allow for greater precision in resist patterning. In 2008, Wang et al. proposed that anion-bonded polymers could reduce anion aggregation, which in turn stabilize the manufacturing process[6]. Their work demonstrated that certain anion-bound polymers could achieve resolutions around sub-50 nm, the standards of modern 5 nm processes in semiconductor manufactory.

Despite these advancements, significant challenges remain. One persistent issue is the inherent randomness in the molecular sizes and compositions of CAR systems, which can cause solubility instability and variations in pattern uniformity. To address these challenges, recent studies have focused on controlling the size and sequence of the polymers used in CAR formulations. For example, in 2022, Kaefer et al. aimed to precisely control polymer size to reduce line edge roughness (LER) and line width roughness (LWR), with the goal of improving overall patterning quality[7–9]. However, these studies are still ongoing, and they have yet to recognize which polymer characteristics are most effective in reducing LER and LWR. A deeper understanding of the molecular mechanisms driving CAR behavior, particularly in EUV processes, remains a significant challenge. Experimental studies face limitations in synthetic techniques that prevent them from quickly identifying the key factors when addressing these issues. This is where molecular dynamics (MD) simulations can provide critical insights, allowing researchers to model the behavior of polymers and photoacids at the atomic level, offering a more detailed understanding of how to optimize resist formulations for EUV lithography[5, 10].

1.3 Overview of this thesis

This thesis aims to address some of the unresolved challenges in the development and application of chemically amplified resists for EUV photolithography through the use of molecular dynamics (MD) simulations. By constructing all-atom models of four distinct

CAR systems, this research seeks to explore the impact of different polymer architectures on chemical distribution and matrix formation. Specifically, the study will focus on comparing block copolymers, random copolymers and anion-bonded polymers, examining how their structural differences influence the matrix structures and distribution of photoacid generators.

One of the primary goals of this research is to provide a detailed analysis of how anion diffusion and uniformity are affected in both free-anion and bonded-anion systems. The study will simulate the behavior of these systems under conditions that mimic formulation of photoresists in actual EUV lithography processes. In expectation, we will gain a deeper understanding of the factors that contribute to pattern roughness and other defects, and to propose potential solutions for improving resist performance. The findings of this thesis will contribute to optimize CARs for future generations of semiconductor manufacturing with shrinking feature sizes and demanding pattern precision.

doi:10.6342/NTU202404559

Chapter 2 Theoretical Background for Molecular Dynamics Simulations

2.1 Periodic Boundary Condition

Although Molecular Dynamics (MD) simulations can model systems much larger than those achievable with quantum mechanical methods, the simulation system is still much smaller compared to real-world systems. Fortunately, ergodic theory ensures that time-averaged properties of a small system can be representative of the ensemble-averaged properties of a much larger system. It allows researchers to simulate a small part of a material over a longer period to obtain statistically significant results. As a result, MD systems are often limited in size, typically in the range of a few hundred nanometers. To avoid artifacts caused by the finite size of the simulation box, periodic boundary condition (PBC) are used. At the boundaries of the system, a replica of the system is placed, connecting with the original system to form an infinitely repeating structure. This method simulates an infinite system by wrapping atoms around the edges of the box, ensuring that surface effects do not dominate the simulation's behavior.

doi:10.6342/NTU202404559

2.2 Development of Force Field

Molecular Dynamics (MD) simulations are a powerful tool for understanding the behavior of atomic and molecular systems by solving Newton’ s equations of motion. At the core of MD simulations is the force field, which approximate the total potential energy of the system by defining how atoms interact with each other. The force field provides an essential framework that includes parameters for both bonded and non-bonded interactions, derived from empirical data or quantum mechanical calculations. These parameters describe the strength of interactions and the preferred molecular structures, simulating the behavior of molecules. In this thesis, general Amber force field (GAFF) was chosen. The following will introduce the simulation methods used in GAFF.

2.2.1 Bonded interactions

Bonded interactions are those that keep atoms connected within molecules, ensuring structural stability. They involve three primary components: bond stretching, angle bending, and torsional forces[11]. Bond stretching describes the energy changes that occur when the distance between two bonded atoms deviates from their equilibrium bond length. This interaction is often modeled using harmonic potentials, which assume that the energy cost increases quadratically as the bond is stretched or compressed. Similarly, angle bending governs the energy associated with deviations from the equilibrium bond angles between three bonded atoms. The potential energy increases as the bond angle shifts from its optimal value, ensuring the molecule maintains its shape.

Torsional forces, or dihedral interactions, are rotational energies within a molecule,

doi:10.6342/NTU202404559

including proper and improper torsions. Proper torsions occur around single bonds between four consecutive atoms (A-B-C-D). These describe the energy changes associated with the rotation around this central bond (B-C). Improper torsions, on the other hand, are used to maintain the planarity of specific groups. These interactions apply to four atoms arranged in a non-sequential fashion, typically to prevent out-of-plane distortions. Improper torsions are often used to ensure that planar structures, such as aromatic rings.

The potential energy of these bonded interactions can be expressed mathematically as a sum of harmonic potentials. For bond stretching, the energy is proportional to the square of the deviation from the equilibrium bond length, while angle bending follows a similar relationship. Torsional forces, on the other hand, are often described by a cosine function, where the energy depends on the dihedral angle ω. The periodicity of the cosine function is determined by the mode of the torsion, denoted by n. The overall bonded energy can be written as:

$$E_{bond} = \sum_{\text{bonds}} \frac{k_b}{2}(l - l_0)^2 + \sum_{\text{angles}} \frac{k_\theta}{2}(\theta - \theta_0)^2 + \sum_{\text{torsions}} \frac{V_n}{2}(1 + cos(n\omega - \gamma)) \qquad (2.1)$$

where k_b and k_θ are force constants for bond stretching and angle bending, l_0 and θ_0 are the equilibrium bond lengths and angles, and V_n represents the torsional potential.

2.2.2 Non-bonded interactions

Non-bonded interactions include Van der Waals and electrostatic interactions. In MD simulations, these interactions are simulated by pairwise potential, with assumption that interaction among group of atoms can be divided into several isolated two-body contributions. Van der Waals forces describe the attractive and repulsive interactions between atoms, modeled using the Lennard-Jones potential. Electrostatic interactions, on the other hand, are modeled with Coulomb potential on point charges. A simple description of the total energy for non-bonded interactions is given by:

$$E_{nb} = \sum_{i=1}^{N} \sum_{j>i}^{N} (4\epsilon_{ij}[(\frac{\sigma_{ij}}{r_{ij}})^{12} - (\frac{\sigma_{ij}}{r_{ij}})^{6]}] + \frac{q_i q_j}{4\pi\epsilon r_i j}) \tag{2.2}$$

where ϵ and σ follow definition in Lennard-Jones potential and $q_i q_j$ are the point charges on atoms i and j.

However, one significant issue arising from the use of PBC is that non-bonded interactions in MD simulations become computationally challenging due to the large number of interacting pairs. To handle this efficiently, cut-off methods are used to approximate Van der Waals forces by considering only nearby atoms. The cut-off distance in the simulations are 1.0 nm. The update scheme of this cut-off method is Verlet limit. On the other hand, the long-range electrostatic interactions are handled using particle mesh Ewald (PME) method. In this method, the point charges of each atom are split into short-range and long-range components. The short-range interactions are calculated in real space, while the long-range interactions are handled in reciprocal space. The charges are projected onto a grid, and then fast Fourier transforms (FFT) are used to compute the cumulative electrostatic potential in reciprocal space. These technique help balance accuracy and computational cost, making it feasible to simulate large molecular systems over extended periods.

2.3 Equation of Motion in MD

In molecular dynamics, the positions and velocities of atoms are controlled by Newton’ s three laws of motion.

$$F_i = m_i a_i \tag{2.3}$$

$$a_i = \frac{d^2 r_i}{dt^2} \tag{2.4}$$

However, molecular dynamic is a many-body problem, which can’ t be solved analytically. As a result, the potential are considered pairwise and finite difference method are used to help increase calculating efficiency. The finite difference method in MD often consider time separated into several fixed-size fragment. Then the force and momentum on each atom can be calculated, to determine the accelerations, velocities, and positions of atoms at each frame. To adopt fixed-size time fragments, most of the algorithms approximate the position-time relation as Taylor series expansions to second order.

$$r(t + \delta t) = r(t) + v(t)\delta t + \frac{1}{2}a(t)\delta t^2 \tag{2.5}$$

A widely-used algorithm is the leap-frog algorithm. Leap-frog algorithm is a finite difference method in molecular dynamics. The basic considerations are as follows:

$$\frac{F}{m} = a(t) = \frac{v(t - \frac{\delta t}{2}) - v(t + \frac{\delta t}{2})}{\delta t} \tag{2.6}$$

First, the acceleration at time is calculate from the interactions between atoms, and

doi:10.6342/NTU202404559

the velocity at $t+\frac{1}{2}\delta t$ could be derived from equation 2-6 with an initial velocity at $t-\frac{1}{2}\delta t$.

$$r(t+\delta t) = r(t) + v(t+\frac{\delta t}{2})\delta t \tag{2.7}$$

Second, the positions at $t + \Delta t$ can be deduced from the velocity at $t + \frac{1}{2}\Delta t$ and the positions at t through equation 2-7. The positions leap over velocities to give their new values, and that derive an obvious disadvantage in calculations of the total energies. Since the velocities and positions are not synchronous, the kinetic energies and position energies could never contribute to the same snapshot in the continuous dynamics. As a result, we only utilize leap-frog algorithm for sampling structures.

2.4 Thermostat and Barostat

The simulations in this study employed several systems within the NPT ensemble. The NPT ensemble refers to systems where the number of particles (N), pressure (P), and temperature (T) are held constant. Achieving these conditions in a simulation requires special algorithms known as thermostats and barostats, which regulate the temperature and pressure respectively.

2.4.1 Thermostat

A thermostat is an algorithm that maintains a constant temperature by controlling the kinetic energy of the particles in the system. The kinetic energy is directly related to temperature through the equation:

$$\langle E_k \rangle = \frac{3}{2}Nk_BT = \frac{1}{2}\left\langle \sum_i m_i v_i^2 \right\rangle \tag{2.8}$$

doi:10.6342/NTU202404559

where N is the number of particles, k_B is the Boltzmann constant, and T is the temperature[12].

In this study, I adopted the Berendsen thermostat, which weakly couples the system to an external heat bath to adjust the temperature. This method allows for a smooth and controlled regulation of temperature, aligning the gradual temperature changes observed in real-world materials, where

$$\frac{\delta T}{\delta t} = \frac{1}{\tau}(T_{bath} - T(t)) \tag{2.9}$$

with τ as the time constant of the system, determining the rate of heat transfer.

The Berendsen thermostat works by rescaling the velocities of the particles to control the temperature[13]. The system temperature T is adjusted over time according to the following relation:

$$T(t + \Delta t) = T(t) + \frac{\Delta t}{\tau}(T_{bath} - T(t)) \tag{2.10}$$

One drawback of the Berendsen thermostat is that it suppresses fluctuations in kinetic energy, which can result in an unrealistic representation of velocity distribution. However, in the large systems studied in this thesis, the error is not significant. Therefore, for the sake of computational efficiency, I chose to employ the Berendsen thermostat in my simulations.

2.4.2 Barostat

The barostat is responsible for maintaining the pressure in molecular dynamics (MD) simulation systems. Pressure in these systems is determined by the positions and interactions of atoms. In realistic physics, pressure is the amount of momentum that cross a unit area in unit time, which is composed of two part of momentum. One is the momentum-related part (P_m), and another is the force-related part (P_f)[12]. For the partial pressure in the x-direction, we can write it as the following equation:

$$P_x = \frac{1}{A}\frac{d(mv_x)}{dt} = P_{mx} + P_{fx} \tag{2.11}$$

The momentum-related part of pressure is represented by the momentum carried by the atoms, which is directly controlled by their velocities. This component of pressure arises from the individual motions of the atoms and is independent of the intermolecular interactions. It is characteristic of ideal gas system, where particles are assumed to be point masses with no interactions. In the ideal gas law, the relationship between pressure, volume, and temperature is described as:

$$\langle E_k \rangle = \frac{3}{2}NkT = \frac{3}{2}P_m V \tag{2.12}$$

$$P_m = \frac{3\langle E_k \rangle}{2V} \tag{2.13}$$

The force-related part is the momentum caused from the the interactions acting between atoms[12]. Since these interactions are simulated through various pairwise potentials, the force acting between two atoms can be identified as a pairwise vector. The force-related pressure act along x-axis can be expressed as:

$$P_{fx} = \frac{\langle F_{fx} \rangle}{A} = \frac{1}{V}\left\langle \int_0^L \sum_i \sum_j F_{xij}\,dx \right\rangle = \frac{1}{V}\left\langle \sum_i \sum_{j>i} F_{xij} x_{ij} \right\rangle \tag{2.14}$$

In this expression, P_{fx} denotes the force-related pressure, while F_{xij} refers to the x-axis projection of the interaction force between atoms i and j. The variable L represents the box length perpendicular to the unit area A, and x_{ij} is the x-axis projection of distance between atoms i and j. The volume of the system is denoted by $V = AL$.

Next, considering the contributions along the x, y, and z axes, the average pressure can be expressed as:

$$P_f = \frac{1}{3}\Big(P_{fx} + P_{fy} + P_{fz}\Big) = \frac{1}{3V}\left\langle \sum_i \sum_{j>i} F_{ij} \cdot r_{ij} \right\rangle \tag{2.15}$$

Finally, combining two part of pressure, the total pressure P can be expressed as:

$$P = \frac{2\langle E_k \rangle}{3V} + \frac{1}{3V}\left\langle \sum_i \sum_{j>i} F_{ij} \cdot r_{ij} \right\rangle \tag{2.16}$$

Like thermostat, I adopted the Berendsen scheme of barostat[14]. It works by rescaling the box volume according to the difference between the instantaneous pressure $P(t)$ and the bath pressure P_{bath}. The volume scaling is governed by the equation:

$$\frac{\delta P}{\delta t} = \frac{1}{\tau_P}(P_{bath} - P(t)) \tag{2.17}$$

where τ_P is the time constant for pressure relaxation, and $P(t)$ is the instantaneous pressure. The scaling factor of volume can thus be derived from compressibility.

$$\beta = \frac{-1}{V}\frac{\partial V}{\partial P} \tag{2.18}$$

$$r + \Delta r = \sqrt[3]{V + \Delta V} \approx \sqrt[3]{V}(1 + \frac{\Delta V}{3V}) = \sqrt[3]{V}(1 - \frac{\beta \Delta P}{3}) \tag{2.19}$$

$$\mu r = r + \Delta r = (1 - \frac{\beta \Delta P}{3})r \tag{2.20}$$

By unphysically rescaling the box length, the barostat couples the system to a pressure bath. The Berendsen barostat, similar to the Berendsen thermostat, does not maintain the correct ensemble distribution. However, this issue is negligible in large simulation systems. The algorithm is considered suitable due to its effectiveness.

doi:10.6342/NTU202404559

Chapter 3 Mathematical Methods for Analysing Polymers and PAGs

3.1 Polymer Structures Analysis

3.1.1 Polymer models and parameters

In polymer physics, end to end distance have often been used to analyze mechanical properties in polymer materials[11, 15]. The end-to-end distance of a polymer refer to its straight-line distance between backbone atoms on both ends, which can be describe from end-to-end vector.

$$|R_{ee}| = \sqrt{R_{ee}^2} \tag{3.1}$$

Consider an ideal polymer (freely jointed model), whose bond lengths on its backbone are fixed to l, and bond angles are fixed to θ. Also, interactions among backbone atoms are ignored, leading to equivalently distributed torsion angles on backbone. For an ideal polymer with n backbone atoms, its end-to-end vector is the sum of all $n - 1$ bond vectors on the chain.

$$R_{ee} = \sum_{i}^{n-1} r_i \tag{3.2}$$

Therefore, the end-to-end distance of an ideal polymer can be written as $\sqrt{l^2 \sum_i \sum_j \langle \cos\theta_{ij} \rangle}$, where θ_{ij} refers to the angle between bond vectors $\vec{r_i}$ and $\vec{r_j}$.

$$\langle R_{ee}^2 \rangle = \left\langle \left(\sum_{i=1}^{n-1} r_i \right) \cdot \left(\sum_{j=1}^{n-1} r_j \right) \right\rangle = l^2 \sum_i \sum_j \langle \cos\theta_{ij} \rangle \tag{3.3}$$

If the bond vectors on backbone of ideal polymer are unrelated, the trajectory of backbone can be considered as simple random-walk. In that case, $\langle \cos\theta_{ij} \rangle_{i \neq j} = 0$, and by definition $\theta_{ii} = 0$, $\cos\theta_{ii} = 1$. The ideal end-to-end distance is defined as:

$$|R_{ee}| = \sqrt{R_{ee}^2} = \sqrt{(n-1)l^2} \tag{3.4}$$

I also employed the concept of persistence length in simulations with all-atom models. The persistence length is a parameter defined to quantifies the ability for polymer chain to maintain its direction[16]. This parameter was initially designed based on the ideal polymer chain, where the bond lengths and angles along its backbone are fixed, and the torsion angles are uniformly distributed. To define the persistence length, the correlation among the bond vectors in the chain needs to be quantified[15].

$$C(m) = \langle \cos\theta_m \rangle = \frac{\sum_i^{n-m} \langle \cos\theta_{i(i+m)} \rangle}{n-m} \tag{3.5}$$

For each segment lengths (m) on the polymer backbone, the angles ($\cos\theta_m$) between bond vectors with similar segment lengths are averaged.

In ideal chain model, since bond angles are fixed to θ, the correlation among bond vectors can be written as:

$$C(m) = \langle \cos \theta_m \rangle = \langle \cos^m \theta \rangle \tag{3.6}$$

With $m = 0$, $C(m)$ is set 1 by definition, and as $m \to \infty$, $C(m)$ will approach 0. The derivative of $\cos^m \theta$ with respect to m is a simple mono-exponential decay. Subsequently, I fitted the correlation function using exponential decay, where m_x represents the difference in the number of polymer units where polymer chain begins to bend.

$$C(m) = \exp \frac{-m}{m_x} \tag{3.7}$$

The persistence length can be derived from $l_p = m_x \cdot l_b$, where l_b is the fixed bond length. Thus, the correlation function can be rewrite as following.

$$C(m) = \exp(\frac{-m l_b}{l_p}) \tag{3.8}$$

For a extremely long and flexible polymer chain, its behavior can be close to this simple model. Nonetheless, in most systems, polymer chains are much deviated. Besides from the flexible bond lengths and angles, the torsion angles (ψ) are not equivalently distributed. The torsion angles are governed by the torsional potential ($U(\psi)$). The torsional potential in polymer matrix system is affected not only by intramolecule interactions (U_{intra}) but also by interactions with the neighboring polymer units, other solutes and solvent molecules (U_{inter}).

$$U(\psi) = U_{intra}(\psi) + U_{inter}(\psi) \tag{3.9}$$

The complexity inherent in $U_{inter}(\psi)$ poses significant challenges when attempting to predict persistence lengths using ideal models. This complexity arises from the intricate interactions and dependencies embedded in $U_{inter}(\psi)$, which makes it difficult to derive accurate predictions without sophisticated approaches. Despite these challenges, a valuable alternative exists: the probability distribution of the variable ψ can be effectively obtained through molecular dynamics simulations. By conducting MD simulations, I can directly compute the probability distribution of torsion angles, $P(\psi)$. [17]. As a result, the same trajectories used for analyzing the end-to-end distance were selected for determining the persistence length.

$$P(\psi) = \frac{\exp(-U(\psi)/kT)}{\int \exp(-U(\psi)/kT)d\psi} \tag{3.10}$$

To calculate the persistence length of each polymer using MD simulations, I first measured the averaged bond length of each bond vector within the polymer. After averaging over 29 different kinds of bond vectors, I obtained a final bond length ($\bar{l_b}$) of 0.269 nm. Next, I calculated the bond vectors along each polymer backbone and measured the angle between vectors separated by m segment lengths. Using the above formula, I then determined the correlation among the bond vectors. Persistence lengths are extracted by fitting to mono-exponential decay function.

3.1.2 Polymer shape identification using gyration tensor matrix

The analysis of polymer shape is complex due to factors such as the arrangement of polymers within the system, the irregular trajectory of their backbones, and the angular relationships between side chains. These complexities make it difficult to classify and analyze polymer shapes. To simplify this issue, I decided to focus primarily on the distri-

doi:10.6342/NTU202404559

bution of the backbone atoms to observe the polymer shapes. By performing regression analysis on the positions of backbone atoms, we can identify the best-fit ellipsoid. The three axes of this ellipsoid can be used to analyze the extent of polymer expansion or contraction[18]. Additionally, the orientation of the ellipsoid's major axis can be utilized to examine the anisotropicity within the polymer matrix. The size of this ellipsoid reflects the extent to which the polymer influences its surroundings while moving within the system.

I use the gyration tensor constructed from backbone atoms to estimate the size and shape of the ellipsoid. The gyration tensor is defined as the covariance matrix of the distance from inertia to each backbone atoms:

$$S = \frac{1}{N}\begin{bmatrix} \sum_i (x_i - x_{cm})^2 & \sum_i (x_i - x_{cm})(y_i - y_{cm}) & \sum_i (x_i - x_{cm})(z_i - z_{cm}) \\ \sum_i (x_i - x_{cm})(y_i - y_{cm}) & \sum_i (y_i - y_{cm})^2 & \sum_i (y_i - y_{cm})(z_i - z_{cm}) \\ \sum_i (x_i - x_{cm})(z_i - z_{cm}) & \sum_i (y_i - y_{cm})(z_i - z_{cm}) & \sum_i (z_i - z_{cm})^2 \end{bmatrix} \tag{3.11}$$

By diagonalizing the gyration tensor matrix, I essentially rotate and scale the principal axes of an ellipsoid in Cartesian coordinates to best fit the distribution of backbone atoms in space.

$$P^{-1}SP = diag(\lambda_1, \lambda_2, \lambda_3) \tag{3.12}$$

$$P = \begin{bmatrix} \nu_1 & \nu_2 & \nu_3 \end{bmatrix} \tag{3.13}$$

The eigenvectors (ν_i) produced by this matrix represent the three principal axes of the best-fit ellipsoid, while the eigenvalues (λ_i) correspond to the root mean square of the ellipsoid's radii[18]. By analyzing the long axes of the ellipsoids, I obtained the vectors for the main direction of each polymer backbone.

3.2 Methods for PAG Distribution Examination

3.2.1 Radial distribution function

The radial distribution function (RDF) between particles of type A and B is defined as:

$$g(r) = \frac{1}{\rho_B} \frac{1}{N_A} \sum_{i \in A} \sum_{j \in B} \frac{\delta(r_{ij} - r)}{4\pi r^2} \tag{3.14}$$

where ρ_B represents the average density of particles of type B, N_A is the total number of particles of type A. The RDF can be further approximated as:

$$g(r) = \frac{\rho(r)}{\rho_0} \tag{3.15}$$

where $g(r)$ represents the radial distribution function, $\rho(r)$ is the local density at distance r from a reference particle, and ρ_0 is the average density of particles in the system[19]. Peaks and valleys in the RDF represent distances where particles are either more or less likely to occur. The larger the amplitude of these features, the more pronounced the structure between the two types of particles and the stronger the interaction.

3.2.2 Coordination number

I employed a switching function to measure the coordination numbers of PAG, defined as following formula, where i represents TPS, j represents anion , r_{ij} represents the intermolecular distance between TPS and anions, and R denotes the critical distance of the switching function [20].

$$N_c^i = \sum_j \frac{1 - (\frac{r_{ij}}{R})^6}{1 - (\frac{r_{ij}}{R})^{12}} \tag{3.16}$$

In an infinitely extended MD system, the minimum distances between all TPS and all anions are converted into their corresponding contributions to the coordination number. For each TPS, an anion within the critical distance R contributes approximately 1, while an anion outside this distance contributes approximately 0. Summing these values yields the coordination number of the given TPS.

3.2.3 Analysis of Moran's I

Moran's I is a spatial statistical index that quantifies the degree of clustering within a system. To use this index, the system must first be divided into equal-sized grid cells, referred to as the resolution, and then the number of the target within each cell is calculated. The index is defined by the formula:

doi:10.6342/NTU202404559

$$I = \frac{N}{\sum_i \sum_j w_{ij}} \frac{\sum_i \sum_j w_{ij}(x_i - \bar{x})(x_j - \bar{x})}{\sum_i (x_i - \bar{x})^2} \tag{3.17}$$

, where x_i represents the number of target in each box, $\bar{x}$ is the mean number of target per box, and w_{ij} denotes the spatial connectivity between boxes (0 or 1). The factor N corresponds to the total number of boxes considered in the analysis.

A zero value of Moran's I indicates a completely uniform distribution of ions throughout the system. A higher Moran's I value suggests a greater degree of clustering of ions, while a lower value reflects a regular alternating pattern of ions.

3.2.4 Ion clustering

Clustering of ions reveals the ion aggregation of the system[19]. I roughly consider the positions of PAG and anion as their sulfur atoms because these atoms are very close to the center of mass of the molecules. In order to construct the algorithm of clustering, I first calculated the pair distance matrix for all sulfur atoms. And then, I tested multiple critical distances for cluster determination. In detail, the critical distance determine whether two atoms belong in the same cluster. When the distance between two sulfur atoms is less than the critical distance, they are classified into the same cluster. This process continues until the distances from any atom from atoms outside the cluster are all farther than the critical distance.

3.3 Mean square displacement and diffusion coefficient

For each atoms, the displacement vector is calculated as the difference between the atom’ s position at two different time steps, represented as $\vec{r}(t) - \vec{r}(t_0)$, where $\vec{r}(t)$ is the position of the atom at time t, and $\vec{r}(t_0)$ is the position at the reference time t_0. The mean square displacement (MSD) is then calculated in each time step, as shown in the following formula, where N is the number of atoms in the selected group.

$$\text{MSD}(t) = \frac{1}{N}\sum_{i}^{N}\left[r(t) - r(t_0)\right]^2 \tag{3.18}$$

According to the Einstein relation, the MSD and time are linearly related by $\lim_{t \longrightarrow \text{inf}} \text{MSD}(t) = 6Dt$, where D denotes the diffusion coefficient.

doi:10.6342/NTU202404559

doi:10.6342/NTU202404559

Chapter 4　MD Simulations

To evaluate the impact of the chemical structure of EUV CAR on material distribution non-uniformity is investigated, four model systems are designed to analyze the effects of various factors, including the ordering of polymer units, the presence or absence of PAG bonding, and the size of anions.

4.1　Model CAR Systems

The substances involved in the photoresist reactions can be simplified into three main categories: the polymer base, the PAG, and the acid quencher that prevents excessive diffusion of the photoacid. In these systems, to better observe the distribution of different anions, we chose not to include the commonly used acid quencher in the resist to reduce the number of variables.

Regarding the polymer, three types of monomers are selected, as shown in Figure 4-1. The first type (unit A) represents a common sensitizer in photoresists, with a phenol side chain. This unit can enhance the EUV absorption in polymer resists. The second (unit B) and third (unit C) types are two different protecting groups. Each unit contains two carbon atoms that are part of the backbone. These units will be catalytically deprotected upon contact with photoacid, exposing polar carboxylate groups. The protecting groups

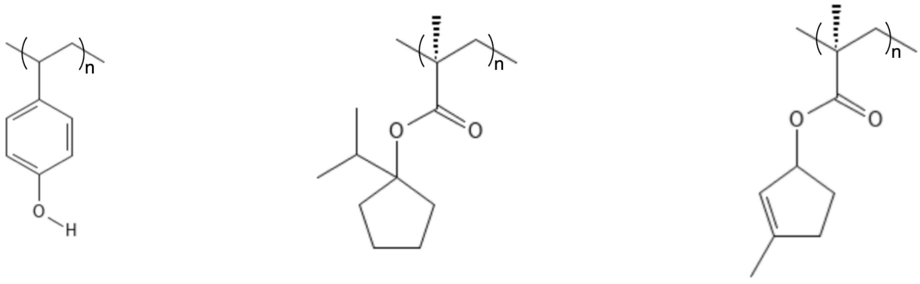

(a) unit A (b) unit B (c) unit C

Figure 4.1: Structures of monomers

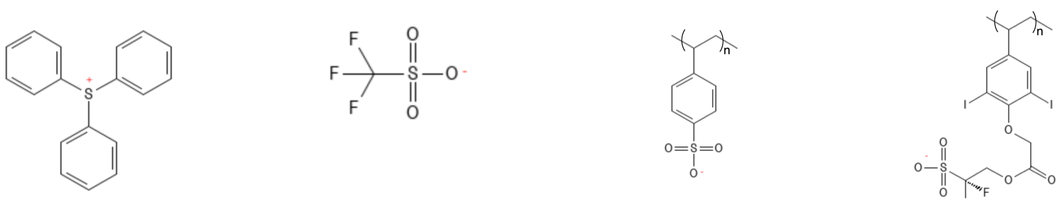

(a) TPS (b) triflic acid (TFL) (c) bonded-anion D (d) bonded-anion E

Figure 4.2: Structures of PAGs

differ in alkyl positions, with unit B having a broader protecting group and unit C having a longer one. For the PAG, the cation selected is Triphenylsulfonium (TPS), and the anions are categorized into free anions and bonded anions to study their ion distribution. The PAG structure is shown in Figure 4-2.

We designed four categories of polymer matrix with different structures based on above: block copolymer with free anion (Rgl), random copolymer with free anion (Rdm), block copolymer with small and rigid bonded-anion (Bsb), and block copolymer with long and flexible bonded-anion (Idd). As illustrated in Figure 4-3, the red ball represents unit A, the green ball represents unit B, the blue ball represents unit C, and the purple ball represents the bonded anions.

In terms of polymer sequences, block copolymers consist of 15 sensitizers (unit A) followed by 15 protected units (9 unit B and 6 unit C), while random copolymers are

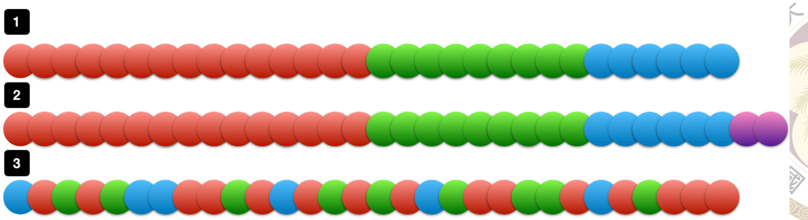

Figure 4.3: Sequence of simulated polymers

composed of the same 30 units arranged randomly, resulting in 128 different sequences. These two types of sequences allow us to compare the effects of phase separation within the polymer. Additionally, units B and C contain chiral centers. For constructing the polymers, unit B was chosen as 6R- and 3S-configurations, and unit C with 2R- and 4S-configurations. In the fixed-sequence polymers (Rgl, Bsb, and Idd), the permutations were fixed as RSRRRSRRS and SRSRSS. Polymers with free anions are fixed at 30 units, while bonded-anion systems have an additional two units at the end, leading to a total of 32 units. The presence of PAG−polymer bonding can be used to observe how the uniformity of ion distribution is affected. Comparing the Bsb and Idd systems will help us understand the effect of anion size.

4.2 GAFF for CAR simulation

After determining the structure of the photoresist, it is necessary to select the appropriate model for simulation. Due to the advancements in the semiconductor industry, which require chip resolutions below 10 nm, a coarse-grained model is unsuitable for simulating chemical phenomena at this scale. Therefore, all-atom models are determined to establish simulations for the EUV CAR matrix. However, we could not find an all-atom force field specifically for photoresist polymers. Consequently, we selected a more general force field, the General Amber Force Field (GAFF), which can be used for most polymers and complex organic compounds[21].

The GAFF was first published in 2004. It is based on the long-established AMBER force field, which was originally designed to streamline the study of biological systems, particularly in drug design[22]. However, GAFF also encompasses a wide range of complex organic compounds beyond common biomolecules. Consequently, it has been applied to many other systems and is highly compatible with most systems in organic chemistry[23, 24].

4.2.1 Atom types in CAR models

In GAFF, atoms are categorized based on their element type, bonding order (or bond type), and placement within specific functional groups. These categorizations further define various atom types, each with its own set of parameters for force field calculations. In our system, excluding the bonded anions, the backbone of the polymers consists of sp^3-hybridized carbon and hydrogen atoms. For the side chains, the sensitizers (unit A) contain phenol functional groups, while the protecting groups (units B and C) feature ester functional groups and more complex aliphatic groups. These functional groups are common and well-defined in GAFF. I used the ACPYPE server, which is based on the ANTECHAMBER program, to convert the atoms to their respective atom types. The corresponding atom types and their structural relationships for the polymers are presented in Table 4-1.

Regarding PAG, all systems use TPS as the cation, while the anion varies depending on the system type. TPS is composed of a sulfur atom bonded to three phenyl rings. The hypervalent sulfur bonded to the three groups is defined as ’s4’ in GAFF. In all types of

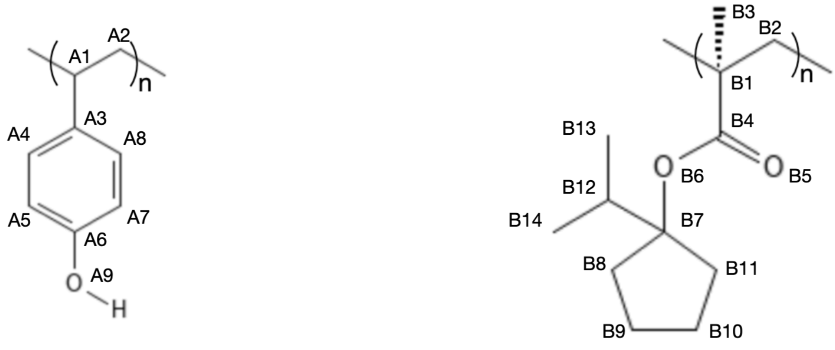

(a) unit A

(b) unit B

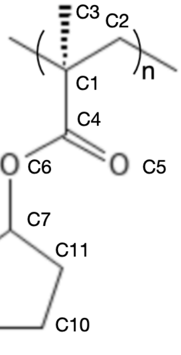

(c) unit C

Figure 4.4: Atomic id of monomers

anions, the sulfurs and oxygens in the sulfonate group are defined as 's6' and 'o', respectively. Their detailed atom type definitions are presented in Table 4-2.

4.2.2 RESP determination of atomic partial charges

In addition to determining the atom type, we also need to decide on the atomic charge for each atom. These atomic charges are not determined by the atom type because they influence different interactions. Atom type determines the bonding interactions and van der Waals interactions of an atom, primarily controlling the bond strength and equilibrium position with neighboring atoms. In contrast, atomic charge determines the molecule' s

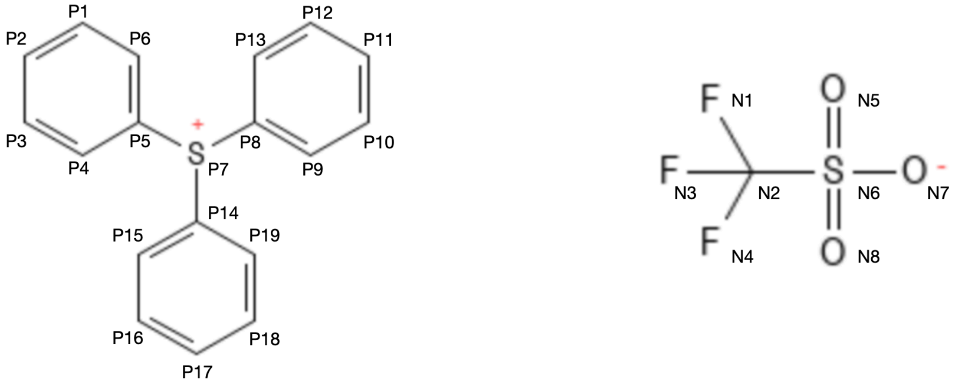

(a) TPS

(b) TFL

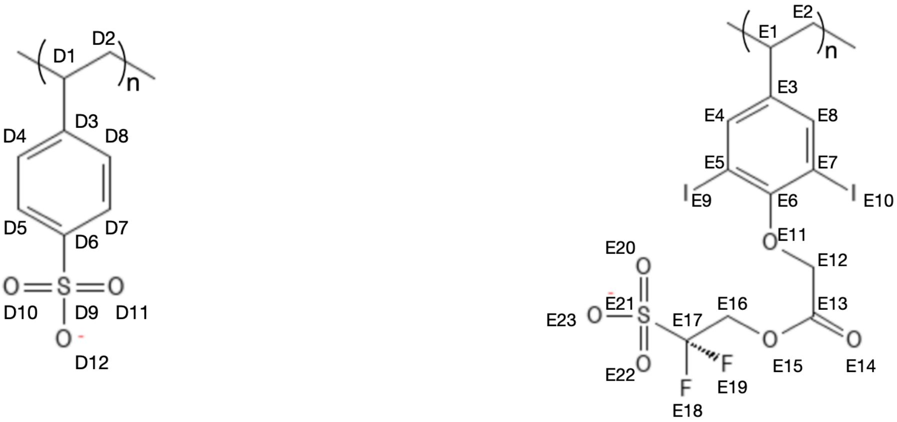

(c) bonded-anion D

(d) bonded-anion E

Figure 4.5: Atomic id of PAGs

Table 4.1: Atom types of polymers

atom id	atom type								
A_1	$c3$	A_{5h}	ha	B_9	$c3$	B_{12h}	hc	C_{10}	$c3$
A_2	$c3$	A_{7h}	ha	B_{10}	$c3$	B_{13h}	hc	C_{11}	$c3$
A_3	ca	A_{8h}	ha	B_{11}	$c3$	B_{14h}	hc	C_{12}	$c3$
A_4	ca	A_{9h}	ho	B_{12}	$c3$	C_1	$c3$	C_{2h}	hc
A_5	ca	B_1	$c3$	B_{13}	$c3$	C_2	$c3$	C_{3h}	hc
A_6	ca	B_2	$c3$	B_{14}	$c3$	C_3	$c3$	C_{7h}	$h1$
A_7	ca	B_3	$c3$	B_{2h}	hc	C_4	c	C_{8h}	hc
A_8	ca	B_4	c	B_{3h}	hc	C_5	o	C_{10h}	hc
A_9	oh	B_5	o	B_{8h}	hc	C_6	os	C_{11h}	hc
A_{1h}	hc	B_6	os	B_{9h}	hc	C_7	$c3$	C_{12h}	hc
A_{2h}	hc	B_7	$c3$	B_{10h}	hc	C_8	$c2$		
A_{4h}	ha	B_8	$c3$	B_{11h}	hc	C_9	$c2$		

Table 4.2: Atom types of PAGs

atom id	atom type								
D_1	$c3$	E_1	$c3$	E_{19}	f	P_8	ca	P_{10h}	ha
D_2	$c3$	E_2	$c3$	E_{20}	o	P_9	ca	P_{11h}	ha
D_3	ca	E_3	ca	E_{21}	$s6$	P_{10}	ca	P_{12h}	ha
D_4	ca	E_4	ca	E_{22}	o	P_{11}	ca	P_{13h}	ha
D_5	ca	E_5	ca	E_{23}	o	P_{12}	ca	P_{15h}	ha
D_6	ca	E_6	ca	E_{1h}	hc	P_{13}	ca	P_{16h}	ha
D_7	ca	E_7	ca	E_{2h}	hc	P_{14}	ca	P_{17h}	ha
D_8	ca	E_8	ca	E_{4h}	ha	P_{15}	ca	P_{18h}	ha
D_9	$s6$	E_9	i	E_{8h}	ha	P_{16}	ca	P_{19h}	ha
D_{10}	o	E_{10}	i	E_{12h}	$h1$	P_{17}	ca	N_1	f
D_{11}	o	E_{11}	os	E_{16h}	$h1$	P_{18}	ca	N_2	$c3$
D_{12}	o	E_{12}	$c3$	P_1	ca	P_{19}	ca	N_3	f
D_{1h}	hc	E_{13}	c	P_2	ca	P_{1h}	ha	N_4	f
D_{2h}	hc	E_{14}	o	P_3	ca	P_{2h}	ha	N_5	$s6$
D_{4h}	ha	E_{15}	os	P_4	ca	P_{3h}	ha	N_6	o
D_{5h}	ha	E_{16}	$c3$	P_5	ca	P_{4h}	ha	N_7	o
D_{7h}	ha	E_{17}	$c3$	P_6	ca	P_{6h}	ha	N_8	o
D_{8h}	ha	E_{18}	f	P_7	$s4$	P_{9h}	ha		

electrostatic potential, influencing intermolecular forces. Atomic charge does not affect bonding interactions because GAFF ignores atomic charges within three bonds when calculating potential energy. Therefore, determining atomic charges does not need to be constrained by atom types.

In MD simulations, several empirical methods for determining charges have been developed, such as Gasteiger charges, which are based on the electron affinity and ionization potential of each atom and its surroundings. However, current empirical methods are only suitable for specific molecules and do not apply well to our system. In the original GAFF paper, two more suitable methods for determining atomic charges were mentioned: AM1-BCC (Austin model 1 - bond charge correction) and RESP (restrained electrostatic potential). RESP is a method more aligned with physical intuition[25]. It initially uses HF/ 6-31G* to model the electrostatic field distribution around the molecule and then tries to allocate these fields to atomic contributions. On the other hand, AM1-BCC was developed to reduce computational cost. It works by obtaining Mulliken charges from semiempirical AM1 calculations (based on electron configuration and atomic orbital overlap) and then making corrections based on bond types. Both methods have issues because our system contains heavy atoms like iodine. Both HF and AM1 are not accurate for iodine calculations. Therefore, we ultimately decided to use RESP at the B3LYP/6-31G* level to calculate atomic charges.

My procedure for the RESP method begins with quantum mechanical calculations for structural optimization and electrostatic potential at the B3LYP/6-31G* level using Gaussian09. After obtaining the optimized structure, I use the CHELPG method in Gaussian09 to extract the electrostatic potential distribution around the molecule, with points avoiding the van der Waals radii of the atoms and a resolution of 3.0 pm. This converts the continuous electrostatic potential into several discrete positions. Next, by adjusting the atom charges, we can compare the differences in electrostatic potential at these positions, which is denoted as χ^2_{esp}. Consequently, performing an iteration to minimize χ^2_{esp} theoretically yields a set of atom charges that aligns with the quantum mechanical predictions of the electrostatic potential. However, this approach may lead to a state with excessively high atom charges, where closely packed positive and negative charges could cancel each other out at some point. Therefore, it is necessary to incorporate a restrained function to prevent the atom charges from becoming trapped in such states. The restrained function is defined as follows[25]:

$$\chi^2_{rst} = a \sum_j (\sqrt{q_j^2 + b^2} - b) \tag{4.1}$$

And by definition, $\chi^2_{resp} = \chi^2_{esp} + \chi^2_{rst}$. Performing the iteration to minimize χ^2_{resp} has a greater chance of aligning with quantum mechanical predictions. I use the programs within

Table 4.3: Atom charges of polymers

atom id	charge								
A_1	-0.047	A_{5h}	0.134	B_9	0.0194	B_{12h}	-0.130	C_{10}	0.128
A_2	-0.075	A_{7h}	0.134	B_{10}	0.0194	B_{13h}	0.067	C_{11}	-0.255
A_3	0.162	A_{8h}	0.114	B_{11}	0.034	B_{14h}	0.067	C_{12}	-0.184
A_4	-0.174	A_{9h}	0.365	B_{12}	0.584	C_1	0.165	C_{2h}	0.062
A_5	-0.224	B_1	0.318	B_{13}	-0.363	C_2	-0.247	C_{3h}	0.062
A_6	0.358	B_2	-0.371	B_{14}	-0.363	C_3	-0.247	C_{7h}	-0.013
A_7	-0.224	B_3	-0.371	B_{2h}	0.093	C_4	0.762	C_{8h}	0.158
A_8	-0.174	B_4	0.724	B_{3h}	0.093	C_5	-0.564	C_{10h}	0.025
A_9	-0.554	B_5	-0.559	B_{8h}	0.009	C_6	-0.489	C_{11h}	0.062
A_{1h}	0.053	B_6	-0.606	B_{9h}	-0.025	C_7	0.486	C_{12h}	0.056
A_{2h}	0.019	B_7	0.296	B_{10h}	-0.025	C_8	-0.457		
A_{4h}	0.114	B_8	0.034	B_{11h}	0.009	C_9	0.168		

Antechamber to perform two consecutive iterations, following the procedure outlined in the original paper, with two sets of parameters as described[25].

In our model, the atom charges of small molecules, such as TPS and TFL, can be directly obtained through the above process. However, due to the limit of computational complexity, the polymer is decomposed into distinct monomers (unit A-E), each simulated separately. Additional -CH_3 and -H groups are attached at the linkage points of each monomer to preserve the sp^3 hybridization of the carbon atoms in the monomer units. After obtaining the electric field distribution of these processed monomers, an additional constraint is applied to the original RESP process. We set the net charge of the newly added carbon and the four hydrogens to zero. This ensures that the net charge of the monomer remains neutral after removing these extra groups. Additionally, it has been confirmed that the charges of these removed groups, even when calculated for different monomers, are similar when computed with the constraint. The final atom charges are presented in Table 4-3 and Table 4-4.

Table 4.4: Atom charges of PAGs

atom id	charge								
D_1	-0.127	E_1	0.294	E_{19}	-0.212	P_8	0.100	P_{10h}	0.123
D_2	0.012	E_2	-0.361	E_{20}	0.928	P_9	-0.108	P_{11h}	0.120
D_3	0.228	E_3	0.007	E_{21}	-0.586	P_{10}	-0.053	P_{12h}	0.123
D_4	-0.246	E_4	-0.138	E_{22}	-0.586	P_{11}	-0.062	P_{13h}	0.097
D_5	-0.016	E_5	-0.063	E_{23}	-0.586	P_{12}	-0.053	P_{15h}	0.097
D_6	-0.106	E_6	0.408	E_{1h}	-0.022	P_{13}	-0.108	P_{16h}	0.123
D_7	-0.016	E_7	-0.063	E_{2h}	-0.022	P_{14}	0.100	P_{17h}	0.120
D_8	-0.246	E_8	-0.138	E_{4h}	0.073	P_{15}	-0.108	P_{18h}	0.123
D_9	1.297	E_9	-0.017	E_{8h}	0.073	P_{16}	-0.053	P_{19h}	0.097
D_{10}	-0.718	E_{10}	-0.017	E_{12h}	0.015	P_{17}	-0.062	N_1	-0.209
D_{11}	-0.718	E_{11}	-0.512	E_{16h}	0.002	P_{18}	-0.053	N_2	0.411
D_{12}	-0.718	E_{12}	0.258	P_1	-0.053	P_{19}	-0.108	N_3	-0.209
D_{1h}	0.053	E_{13}	0.643	P_2	-0.062	P_{1h}	0.123	N_4	-0.209
D_{2h}	-0.017	E_{14}	-0.514	P_3	-0.053	P_{2h}	0.120	N_5	-0.659
D_{4h}	0.089	E_{15}	-0.381	P_4	-0.108	P_{3h}	0.123	N_6	1.194
D_{5h}	0.088	E_{16}	0.156	P_5	0.100	P_{4h}	0.097	N_7	-0.659
D_{7h}	0.088	E_{17}	0.352	P_6	-0.108	P_{6h}	0.097	N_8	-0.659
D_{8h}	0.089	E_{18}	-0.212	P_7	0.176	P_{9h}	0.097		

4.3 Initial Structure Preparation

In semiconductor lithography, pattern widths typically range from 10 to 20 nm. Therefore, we plan to set the matrix size as a box with dimensions of 20 x 10 x 20 nm. Based on the composition ratios of photoresists used in semiconductor manufacturing, our system requires a ratio of 1:2 for polymers and photoacid generators (PAGs). Given a resist density of 1, it is estimated that approximately 500 polymers and 1000 PAGs are needed. Generating a matrix with 500 polymers while avoiding human bias is challenging. Previous methods documented in the literature can generate such polymer matrix but are not compatible with our research goals. For instance, the lattice model using a self-avoiding walk often overlooks the specific structure of polymer units and is not easily applicable to fixed-sequence polymers[26] . Therefore, we designed a new method that aligns with physical images.

4.3.1 Polymer matrix formation from gas phase matrix

Initially, we randomly placed 16 polymers and 32 PAGs into a large cavity. To avoid unreasonable contacts between molecules, we applied the steepest descent method for potential energy minimization with GROMACS. This method first requires calculating the gradient ($\nabla f(x)$) of the potential energy surface at the initial configuration (x_0). This gradient indicates the steepest direction on the potential energy surface. We then evolve the initial structure slightly in this direction:

$$x_{k+1} = x_k + \alpha \nabla f(x_k) \tag{4.2}$$

We repeat this process until the new gradient is smaller than 10.0 kJ/mol $\cdot$ nm, at which point we obtain a reasonable structure that is at a local minimum.

After energy minimization, the 16 polymers and 32 PAGs are dispersed in a large cavity with no close interactions between them. This cavity is large enough to be nearly vacuum-like, and due to the considerable distances, the intermolecular attractions are weak, similar to gas phase. As external pressure is gradually increased, the molecules move closer to each other, eventually forming a solid structure.

conditions for simulation (parameters for non-bonded interactions)

Subsequently, we applied high temperature and pressure to liquefy the polymer structure, compressing the polymers and ions together until the system density stabilized, reaching approximately 1 g/cm^3, which is typical for most photoresists used in experiments.

doi:10.6342/NTU202404559

4.3.2 Simulated annealing of polymer matrix

We subjected the system to 100 annealing cycles, each lasting 100 ps, with temperatures varying from 400 K to 1000 K. The permittivity was set to 3 to simulate the actual values of the polymers. This procedure effectively reduced the potential energy of systems and accelerated the equilibration process. The structures after annealing were then relaxed in a 500 K, 1 bar NPT ensemble. Next, because of the periodic boundary conditions, we copied the system and stacked it along the x, y, and z axes, resulting in a system containing 128 polymers and 256 ion pairs. We then performed 100 annealing cycles on this structure to disrupt correlations between polymers and relax it to the 500 K, 1 bar NPT ensemble. Subsequently, the structure was copied and stacked along the x and z axes to achieve 512 polymers and 1024 ion pairs. Finally, the system underwent another round of annealing and equilibration. Throughout these steps, the density of the system remained near 1 g/cm^3 under NPT ensemble conditions at 500 K and 1 bar. It is important to note that the goal of simulated annealing is not to find the global minimum in potential energy of the system but to find a stable structure that is representative of the dynamic equilibrium within the polymer matrix. The potential energy of the Rgl system with 512 polymers after each annealing cycle is presented in Figure 4-6. As illustrated in the figure, after approximately 20 cycles, the system's potential energy exhibits fluctuations within a specific range and maintains this behavior for the remaining 80 cycles. This observation indicates that the system has reached a state of dynamic equilibrium. Consequently, the structures obtained after 100 annealing cycles are regarded as the initial configurations for this system. These structures are then subjected to equilibration in a 500 K, 1 bar thermal bath for 10 ns.

doi:10.6342/NTU202404559

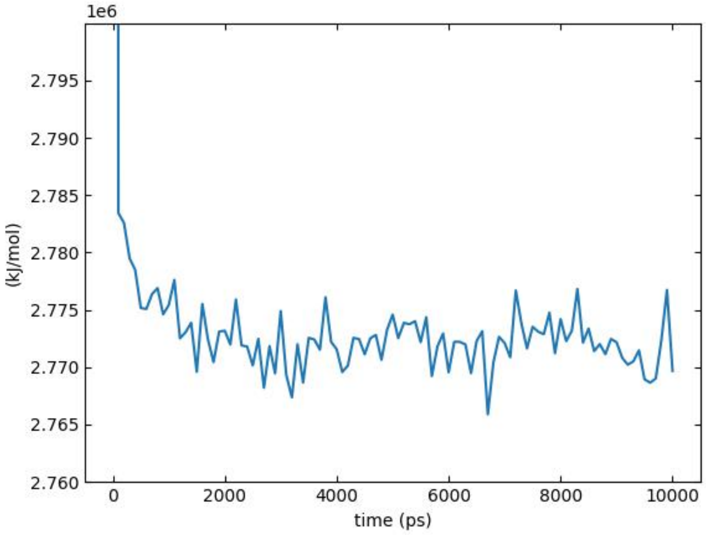

Figure 4.6: Evaluation of potential energy of Rgl PR systems after each annealing cycle

4.4 Verification for Equilibrium State

In MD simulations, achieving complete equilibrium is inherently impossible. This is because, although MD simulations represent a significant improvement in scale compared to quantum mechanics simulations, they still model only a small portion of the system compared to the actual experimental systems. According to ergodic theory, to represent a millimeter-scale chip with a system on the nanometer scale, an exceedingly long simulation time would be required. However, due to limitations in computational resources, simulations are typically limited to nanoseconds. This level of simulation is likely to introduce reasonable statistical errors when compared to large-scale experimental results. Consequently, it is challenging to determine whether 'all' the differences between our simulated and experimental observables fall within acceptable statistical error margins.

Nevertheless, while achieving complete equilibrium is unattainable, MD simulations can reach partial equilibrium[27]. Certain indicators may stabilize to a very consistent state over a certain simulation period and maintain this stability for an extended time.

Table 4.5: Box size of each systems at the final frame of 500K trajectory

System name	x, z length (nm)	y length (nm)	volume (nm^3)
Regular-sequenced polymer (Rgl)	21.41	10.70	4905
Random-sequenced polymer (Rdm)	21.38	10.69	4886
Besylate-bonded polymer (Bsb)	21.44	10.72	4928
Iodine-doped polymer (Idd)	21.82	10.90	5190

The properties represented by these indicators can be considered to have reached equilibrium, thus providing statistically representative results. To ensure equilibrium for specific observables, we conducted an additional simulation for 50 ns at 1bar and 500 K, a temperature exceeding the glass transition temperature (Tg) of most polymer resists. The equilibrium state of the system was confirmed by evaluating the stability of various structural indicators, including the matrix density for overall stability, the polymer radius of gyration for polymer mobility, and the radial distribution function of ions for ion distribution.

During the additional 50 ns of simulation, the density exhibited exceptional stability (Figure 4-7). The densities of the four systems remained close to 1 g/cm^3, which is comparable to the densities of most experimental photoresists. Except for the Idd system, where the polymer’ s larger anion volume resulted in a higher density, the densities of the other systems were similar. The box sizes at the final frame for each system are recorded in Table 4-5.

The radius of gyration of polymer was investigated using the gyration-tensor matrix over a trajectory from 12 ns to 24 ns at 500K. The detailed algorithm is described in Chapter 03. As shown in Figure 4-8, the radius of gyration of the polymer in all four systems reached equilibrium after 12 ns. This indicates that the shape of polymers has

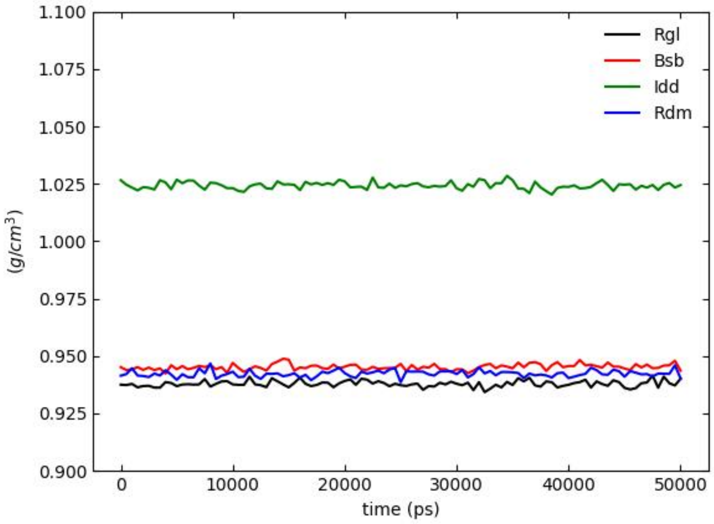

Figure 4.7: Inspection of density for equilibrium

achieved equilibrium.

Regarding ion distribution, the radial distribution function (RDF) between TPS sulfur atoms was monitored every 10 ns over a 50 ns trajectory at 500K. This pair was chosen because it is less controlled compared to anions in all four systems, and thus is expected to reach equilibrium later. Figure 4-9 shows the RDF for the Rgl system as a representative example. The RDF remains stable throughout the entire 50 ns trajectory, indicating that ionic coordination and distribution have reached equilibrium.

4.5 Procedure for Production Run

After verifying the stability of the major indicators in the system, we can confirm that the current simulation time is sufficient for the system to reach equilibrium in terms of density, polymer shape, and ion distribution. Therefore, we can proceed with the production run of the MD simulation to analyze the effects of various factors on the system.

During post-exposure bake (PEB), photoresists are subjected to heating processes,

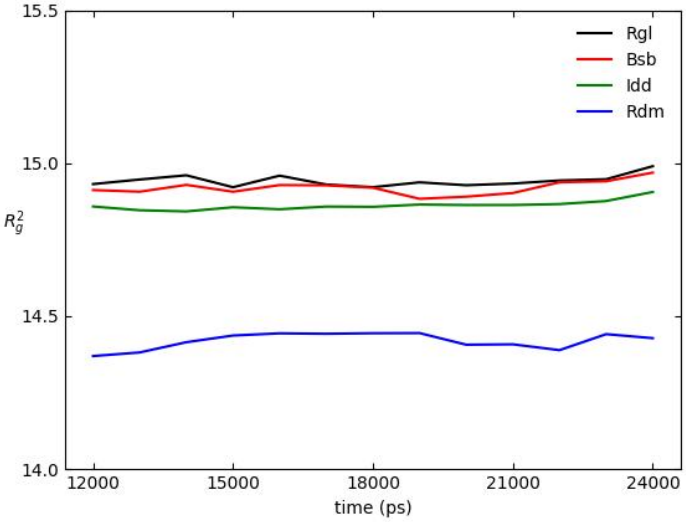

Figure 4.8: Inspection of Rg2 for equilibrium

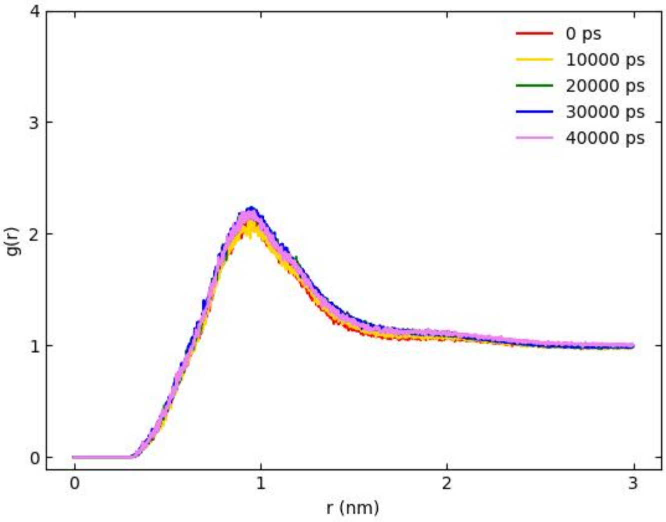

Figure 4.9: Inspection of radial distribution function from TPS sulfur to TPS sulfur for equilibrium

doi:10.6342/NTU202404559

typically ranging from 360 K to 420 K, to facilitate chemical reactions. Therefore, we aim to observe structural changes in the system during PEB heating. Given the slower rate of structural changes in MD simulations, the simulations were initiated at 400 K and conducted every 10 K up to the polymer's glass transition temperature.For the Rgl and Rdm systems, the temperature range extended from 400 K to 500 K, while for the Bsb and Idd systems, it ranged from 400 K to 540 K. All structures at various temperatures were simulated starting from the same 500 K equilibrium structure for all types of systems. Since the system reaches equilibrium within 10 ns, and to reduce computational resource demands, each MD trajectory at various temperatures lasts 25 ns.

Besides the temperature effect, this study also aimed to clarify the role of bonded anions and the impact of polymer unit sequencing. These two factors will be examined by comparing the four systems.

doi:10.6342/NTU202404559

Chapter 5 Structural Analysis of EUV CAR Polymers

There have been numerous studies on the impact of polymer architecture on LER. In 2004, George et al. claimed that either larger polymers or increased free volume correspond to higher LER[28]. In 2006, they further asserted that the shape of polymers can be a contributing factor to LER. The LER found in linear polymers is smaller than that in randomly grafted polymers. In 2007, Philippou et al. also proposed that larger polymers lead to higher roughness, as the grain size at the edge increases. With controlled sequence and length, the polymer grain size is primarily influenced by its rigidity and shape. These studies indicate that polymer architecture, including size and shape, can affect its dissolution properties and LER[29].

In this chapter, the differences in the polymer matrix structure formed by different polymer compositions will be discussed. In order to understand the architectural differences caused by various polymer structures, the shape of block and random copolymers was investigated by analyzing their end-to-end distance, persistence length, and gyration tensor.

5.1 Rigidity of Polymers

5.1.1 End-to-end distance of CAR polymers

For ideal polymers in random-walk model, the ratio of its end-to-end distance to contour length is $\frac{\sqrt{n-1}}{n-1}$. In our systems, where polymers are composed of 30 or 32 units ($n = 30$ or $n = 32$), the ideal ratio are about 0.2 (0.19 or 0.18). We analyzed the end-to-end distances in CAR systems using MD trajectories at 500K. This temperature is 100K higher than the experimental reaction temperature. We chose this high temperature because it enhance the mobility of polymer chains, which helps the polymer structures approach their ideal configurations. All systems were simulated in the NPT ensemble for 25 ns. For each polymer in the system, the end-to-end distance is determined using the vector defined by the positions of the two carbon atoms at the ends of the polymer backbone. End-to-end distances were recorded every 0.5 ps throughout the trajectory. The ratio of end-to-end distance to its contour length are presented as probability density distributions for the four model CAR systems (Figure 5-1). Table 5-1 records the averaged end-to-end distance and the standard deviation for all systems. In systems with free anions (Rgl and Rdm systems), the contour length of polymers are about 7.8 nm (30 units), while in systems with bonded-anion (Bsb and Idd systems), since attached with two additional anion units, their contour length are about 8.4 nm (32 units). In general, polymers in all systems are highly deviated from the ideal polymer, where most of their end-to-end distance are above 0.2, the ideal ratio to contour length. This is expected because the huge volume of each units and relatively short polymer length can lead to strong excluded volume effect.

In comparison, the averaged end-to-end distance in Rdm system, is shorter than that

Table 5.1: Calculated end-to-end distance in four systems

System name	Average (nm)	Standard deviation (nm)	Ratio to contour length (%)
Regular-sequenced polymer (Rgl)	3.40	1.19	43.6
Random-sequenced polymer (Rdm)	3.25	1.10	41.7
Besylate-bonded polymer (Bsb)	3.42	1.25	40.7
Iodine-doped polymer (Idd)	3.51	1.17	41.8

in Rgl systems. It shows that random-sequencing of polymer would lower the steric effect between neighboring units, and thus reduce its stiffness. This also implies that specific combination of monomers might contribute extra rigidity on polymers and thus enhance the mechanical strength of matrix. As for bonded-anion systems, the averaged end-to-end distance in Bsb is shorter than that in Idd system. It is because of the smaller volume on Besylate anions. The anions in Idd systems, despite with a flexible side chain, instead lead to more rigid backbones. From their ratio to contour length, most polymers are around 20% to 60%, the standard deviations are about 1.2 nm. The large standard deviation implies various polymer shape in matrix. In summary, bonded-anions does not necessarily affect polymer stiffness. The main factors affecting polymer rigidity is the specific combination on polymer sequence.

5.1.2 Persistence length of CAR polymers

To quantify the rigidity of polymers, we also calculated persistence length with MD trajectories at 500K in these systems. Analyses of persistence length are frequently applied when studying polymers with contour lengths exceeding 50 nm. This focus arises because polymers of this length more closely approximate ideal chains, and their correlation functions resembles mono-exponential decay. However, the polymers we investigated contain

doi:10.6342/NTU202404559

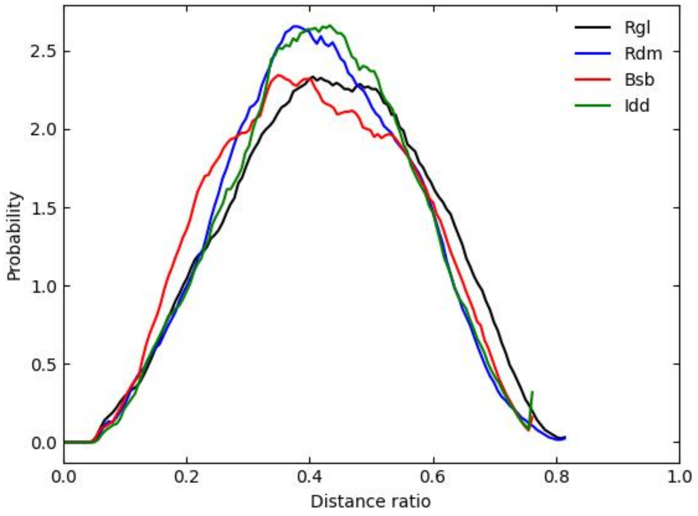

Figure 5.1: Probability of distance ratio

far fewer units. As a result, the persistence lengths obtained in this study are considerably shorter than those typically observed in experimental settings, preventing direct comparisons with experimental data. In our simulations, the persistence lengths were found to be 1.10 nm for block copolymers with free anion (Rgl), 0.93 nm for random copolymers with free anion (Rdm), 1.07 nm for block copolymers with rigid bonded-anion (Bsb), and 1.02 nm for block copolymers with flexible bonded-anion (Idd). A lower persistence length indicates greater propensity for the polymer to bend. As shown in Figure 5-2, random copolymers are markedly softer compared to block copolymers. This flexibility in random copolymers reduces steric hindrance between highly voluminous molecules, facilitating easier bending of the polymer backbone. Regarding bonded-anion systems, the trends among the three types were too similar to draw significant conclusions, indicating minimal influence of anion type on polymer flexibility.

doi:10.6342/NTU202404559

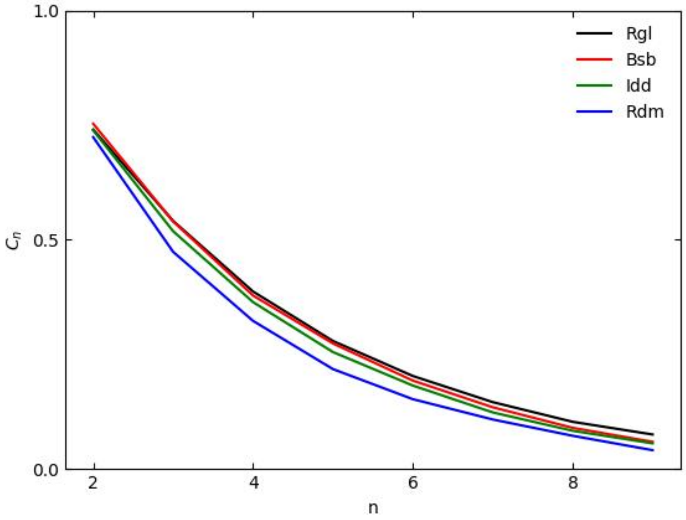

Figure 5.2: Correlation among the bond vectors for each system

5.2 Temperature Dependency of Polymer Shape

From the study of end-to-end distance (Table 5-1), we observed huge variety in the end-to-end distance of CAR polymers, indicating a wide range of polymer shapes. To further understand the architecture of these shapes, the gyration tensor was applied to simulate the ellipsoidal shape of these polymers.[18] In addition, since polymer structures change much more rapidly at high temperatures, particularly above the glass-transition temperature, the temperature-dependency of polymer shapes was investigated. The polymer shapes in free anion systems were analyzed within the temperature range of 400K to 500K, while those in bonded-anion systems were analyzed within the range of 400K to 540K.

5.2.1 Characterization of the shape of CAR polymers

At first, to observe the anisotropy in systems, polymer shapes are analyzed with MD trajectories at 500K. The major axes of polymers with more elongated shapes ($\lambda_1 > 2\lambda_2$)

at 500K are collected as direction vectors of them, where the direction vector is represented by $\vec{\nu}_1 = [\nu_{1x}, \nu_{1y}, \nu_{1z}]$. The variance of these direction vectors of the collected polymers was then compiled into a matrix as following[18]:

$$S = \frac{1}{N} \begin{bmatrix} \sum_i \nu_{1x,i}^2 & \sum_i \nu_{1x,i}\nu_{1y,i} & \sum_i \nu_{1x,i}\nu_{1z,i} \\ \sum_i \nu_{1x,i}\nu_{1y,i} & \sum_i \nu_{1y,i}^2 & \sum_i \nu_{1y,i}\nu_{1z,i} \\ \sum_i \nu_{1x,i}\nu_{1z,i} & \sum_i \nu_{1y,i}\nu_{1z,i} & \sum_i \nu_{1z,i}^2 \end{bmatrix} \tag{5.1}$$

Similar to the gyration tensor, by diagonalizing this matrix, we obtained the best-fit principal axes and the root mean square radii of the polymer dimension vectors within the overall system. As shown in Table 5-2, it is found that the orientation of polymers within the system is nearly random at 500K, where the three eigenvalues are close to each other. It indicates that there is no particularly packing effect between the polymer matrices. Therefore, a relatively flat cross-section cannot be found on the chip, making the chip's line edge more susceptible to changes in the shape of the polymers at the interface.

After confirming the anisotropy of each system, the variability in polymer shapes within the system and the trends in polymer shape as a function of temperature were studied. The mean and standard deviation of the three principal axes were computed for each polymer every 10K, from 400K to above 500K. The three eigenvalues for each system as a function of temperature are plotted in Figure 5-3, where the solid lines represent the average eigenvalues and the dashed lines indicate the standard deviations. In random copolymers (Rdm), the longest axis is shorter, while the shortest axis is longer compared to block copolymers, resulting in a more coiled shape. The effects of different anions, on the other hand, are relatively minor. As the temperature increases, the polymer undergoes

Table 5.2: Eigenvalues and eigenvectors calculated from gyration tensor of polymer backbone

System name	eigenvalues	eigenvectors
Regular-sequenced polymer (Rgl)	$\begin{bmatrix} 38.9 \\ 37.5 \\ 35.7 \end{bmatrix}$	$\begin{bmatrix} 0.64 & -0.41 & 0.65 \\ -0.77 & -0.44 & 0.47 \\ -0.09 & 0.80 & 0.59 \end{bmatrix}$
Random-sequenced polymer (Rdm)	$\begin{bmatrix} 37.0 \\ 36.3 \\ 34.9 \end{bmatrix}$	$\begin{bmatrix} -0.12 & -0.47 & 0.88 \\ -0.92 & 0.39 & 0.08 \\ 0.38 & 0.79 & 0.47 \end{bmatrix}$
Besylate-bonded polymer (Bsb)	$\begin{bmatrix} 39.2 \\ 37.4 \\ 34.9 \end{bmatrix}$	$\begin{bmatrix} -0.45 & 0.85 & -0.28 \\ -0.40 & 0.09 & 0.91 \\ -0.80 & -0.52 & -0.30 \end{bmatrix}$
Iodine-doped polymer (Idd)	$\begin{bmatrix} 38.2 \\ 37.3 \\ 34.5 \end{bmatrix}$	$\begin{bmatrix} 0.87 & -0.46 & 0.17 \\ 0.43 & 0.54 & -0.72 \\ -0.24 & -0.70 & -0.67 \end{bmatrix}$

greater elongation along its longest axis compared to the expansion along the shorter axes. This suggests that temperature aids in stretching the polymer’ s shape. The polymer’ s approximate dimensions are around 3 nm × 2 nm × 1.5 nm, approaching the 3 nm limit of the LER process. Therefore, precise control over the polymer’s shape and arrangement using specific units will enhance process stability.

5.2.2 Shape description from gyration-tensor analysis

Several metrics were applied to assess the polymer’s shape, including the squared radius of gyration (R_g^2), anisotropy (K^2), and deviation from spherical symmetry (b). These indicators are defined by the eigenvalues[18]:

$$R_g^2 = \lambda_1 + \lambda_2 + \lambda_3 \tag{5.2}$$

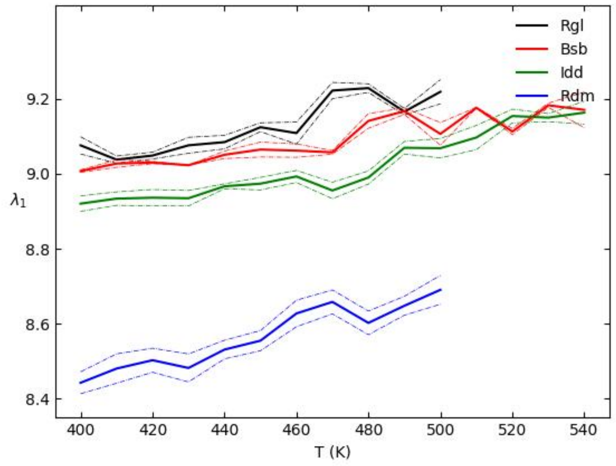

(a) λ_1

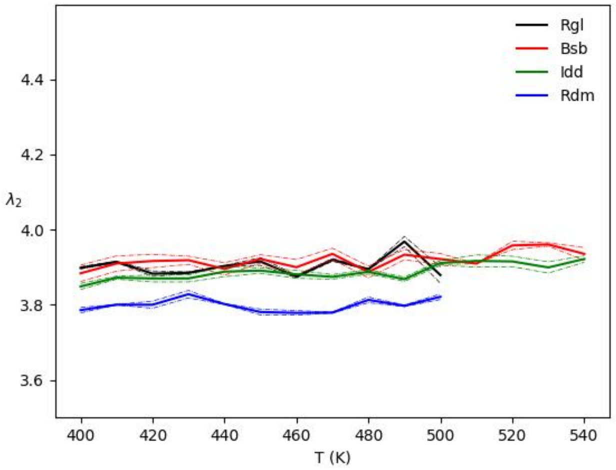

(b) λ_2

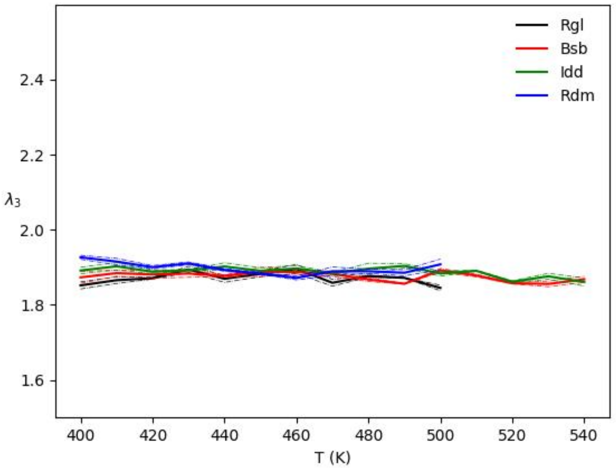

(c) λ_3

Figure 5.3: Estimated eigenvalues of polymer shape at various temperatures from gyration tensor

$$\kappa^2 \equiv \frac{3}{2}\frac{\mathrm{Tr}\hat{S}^2}{(\mathrm{Tr}\hat{S})^2} = 1 - 3\left[\frac{\lambda_1\lambda_2 + \lambda_2\lambda_3 + \lambda_1\lambda_3}{(\lambda_1 + \lambda_2 + \lambda_3)^2}\right] \tag{5.3}$$

$$b = \lambda_1 - \frac{1}{2}(\lambda_2 + \lambda_3) \tag{5.4}$$

As shown in Figure 5-4, both the squared radius of gyration (R_g^2) and the deviation from spherical symmetry (b) are smaller for random copolymers compared to block copolymers, indicating that random copolymers have smaller grain sizes. Additionally, the anisotropy (K^2) of random copolymers is lower than that of block copolymers, suggesting a more coiled polymer shape. These observations lead us to conclude that random copolymers possess a more flexible and plastic structure.

The ellipsoid volumes at various temperatures were also calculated. Since each eigenvalue was the variance derived from the polymer backbone, the estimated volumes can represent the size of the free volume left behind by the calculated polymer after dissociation.

$$V = \frac{4\pi}{3}\sqrt{\lambda_1\lambda_2\lambda_3} \tag{5.5}$$

In Figure 5-5, it is shown that random-sequenced polymers (Rdm) occupy a smaller volume compared to regular-sequenced polymers (Rgl). This indicates that random-sequenced polymers have a smaller grain size within the system, likely due to the influence of their softer backbone. As the temperature increases, the elongation of λ_1 occurs at a faster rate

doi:10.6342/NTU202404559

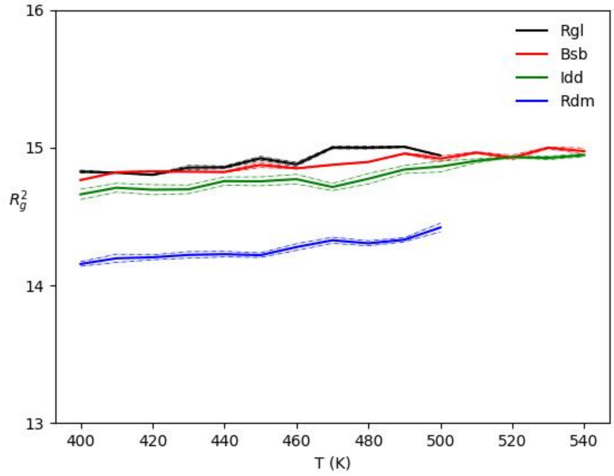

(a) R_g^2

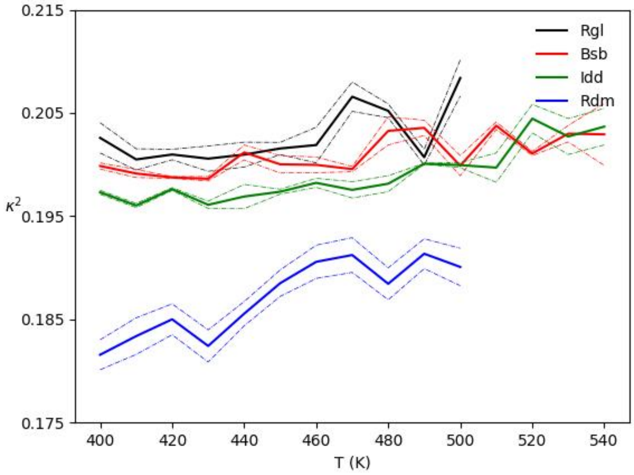

(b) κ^2

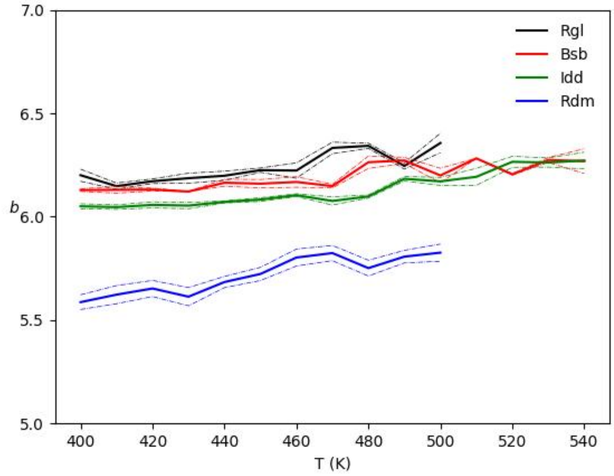

(c) b

Figure 5.4: Shape descriptors of polymers estimated from gyration tensor

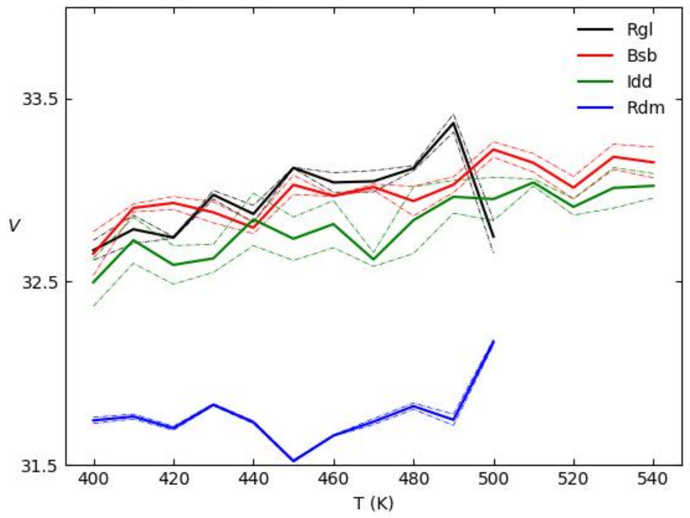

Figure 5.5: Estimated volume of polymer from gyration tensor

compared to the other axes. This leads to an increase in anisotropy (K^2) and deviation from spherical symmetry (b) with rising temperature. More importantly, the ellipsoid's volume also increases. This suggests that during the post-exposure bake process, the polymer’s shape is likely to gradually expand, creating more space for PAGs and other small molecules.

doi:10.6342/NTU202404559

doi:10.6342/NTU202404559

Chapter 6 PAG Distribution in Polymer Matrix

An ideal CAR requires a completely homogeneous PAG distribution. However, achieving this is extremely challenging since the role of anions in these systems is multi-faceted. On one hand, anions need to possess sufficient mobility to increase the number of polymers they can catalyze. On the other hand, this same mobility of the anions causes uneven diffusion in the reaction zone, impacting the linewidth of the substrate[30, 31]. In 2004, simulations conducted by George et al. indicated that acid diffusion smoothens LER but compromises critical dimension control[28].

To address this issue, a commonly used modern approach is to employ a quencher to absorb the protons carried by the anions. However, the effectiveness of this method depends on the properties of both the quenchers and the anions. The concentration of both, as well as their affinity to the polymer structures in the formulation, needs to be tested under experimental conditions. Nevertheless, due to the mobility limitations of the quenchers, their efficacy is also restricted. Another approach involves using anion-bound polymers as a component of the photoresist, which directly limits the distribution of the anions. In 2008, Wang et al. proposed several anion-bonded polymers as a recipe for CAR and claimed that this method enhanced resolution by suppressing anion aggregation[6].

This breakthrough allowed them to surpass the resolution limits of CAR, reaching the 5 nm process. Today, as the industry approaches the 2- or 3-nm process era, it is crucial to gain deeper insights into the relationship between ion aggregation and structure to drive further advancements in CAR. With MD simulation, we can observe the intermolecular interactions within various structures more rapidly.

In this chapter, the distribution of PAGs in bonded-anion systems will be compared with that in free anion systems. To examine ion distribution between free anions and bonded-anions, we employed indicators such as ion cluster analysis, RDF (radial distribution function), number density distribution, and coordination number for comparison.

6.1 Cation-anion Interactions

6.1.1 Radial distribution of cation-anion coordination

To compare the aggregation states of ions, the radial distribution function (RDF) was calculated to examine how the density of ion particles varies with distance from a reference particle, compared to a random distribution. In this study, we selected MD trajectories at 500K to compare multiple radial distribution functions (RDF), including the relationships between TPS sulfur to anion sulfur, anion sulfur to anion sulfur, and TPS sulfur to TPS sulfur across the four systems. At this temperature, all four systems have reached the glass transition temperature, which will be discussed in Section 7-2. It is because polymers are more mobile at glass transition temperature, making the structure less influenced by our initial setup. Comparing under these conditions provides a higher degree of reliability.

From the RDF of TPS sulfur to anion sulfur, we can observe similar structures in

doi:10.6342/NTU202404559

all four systems (Figure 6-1). Within 1 nm, each system exhibited two primary peaks at approximately 4 Å and 6 Å, along with a smaller secondary peak around 9 Å. This pattern arises because all four types of anions fundamentally remain as sulfonate groups, and the electric field environment provided by the polymer matrix is consistent, thus not affecting the interaction between TPS and the anion. The two primary peaks result from the angular orientation between TPS and the anion. When the sulfur of TPS rotates close to the sulfonate group on the anion, a peak forms at around 4 Å. Another peak appears around 6 Å when one end of TPS with three benzene rings approaches the sulfonate group of the anion. The two peaks are caused by cation rotation and should therefore be considered as a splitting of the first shell. The secondary peak at 9 Å overlaps significantly with the 6 Å peak, making it challenging to analyze its origin. However, it is speculated to be influenced by ion aggregation, as this peak is noticeably diminished in the bonded anion systems.

In the RDF of TPS sulfur to TPS sulfur, all four systems displayed similar widths for the first shell, falling within the range of 0.4-1.6 nm, with peak maxima around 1 nm. The peak heights were lower in the anion-bound system, indicating fewer TPS molecules near each other due to dispersed anion distribution. This implies that in anion-bound polymer systems, both cations and anions are more dispersed overall (Figure 6-2). In the RDF of anion sulfur to anion sulfur, we observed that the flexible bonded-anion (Idd) exhibited smaller peaks compared to the free-anion (Rgl), indicating a more dispersed anion distribution, thereby reducing anion aggregation within the photoresist. The rigid bonded-anion (Bsb), being fixed on the polymer backbone, also showed narrower peaks compared to free anion (Rgl), but with increased distances between anions. This suggests that even the artificially designed bonded-anions, structured as dimers, disperse due to

doi:10.6342/NTU202404559

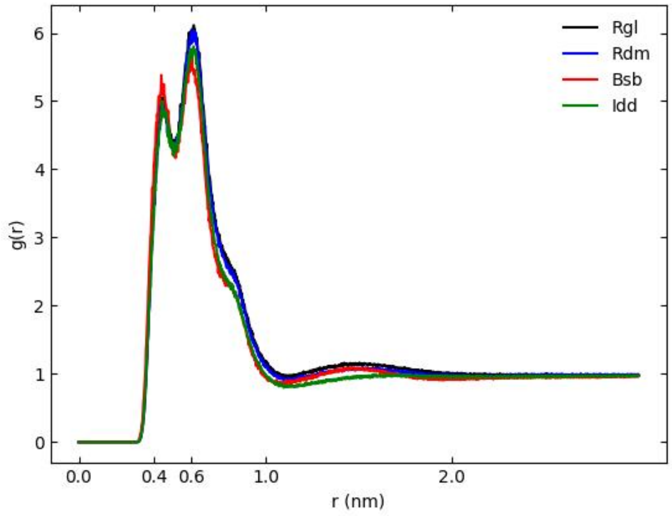

Figure 6.1: Radial distribution function of ion pairs at 500K trajectory

steric effects and Coulomb repulsion, resulting in wider anion distribution.

6.1.2 Coordination number of cation-anion

The extent of aggregation between ion pairs appears similar based on the RDF analysis of anion-TPS interactions. However, the RDF analysis is unable to reveal the degree of variation between individual molecules. Among all ionic interactions, the coordination between TPS and anions is the most critical, as it defines the electric field distribution surrounding the TPS and anions. Therefore, the probability density of their coordination numbers is investigate. Since their first shell is mostly within 1 nm, the coordination numbers for each TPS molecule are calculated with a critical distance of 1 nm.

The analysis was conducted using MD trajectories at 500K, from 3 ns to 24 ns with calculations performed every 3 ns. The statistical results are displayed as a histogram in Figure 6-3. The theoretical average value of N_c indicates the extent to which TPS molecules are subjected to a negative electric field. When more anions coordinate, the

doi:10.6342/NTU202404559

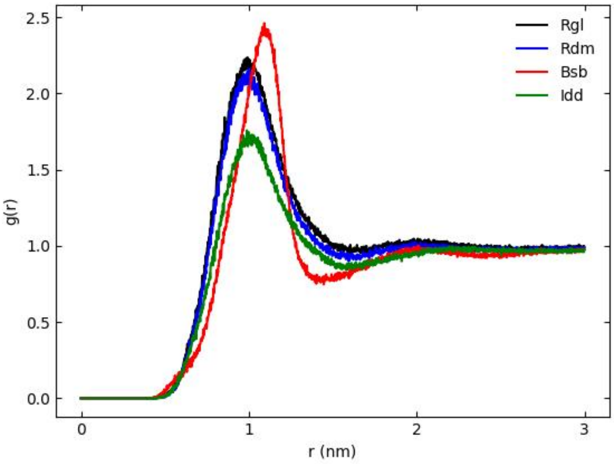

(a) anion-anion rdf

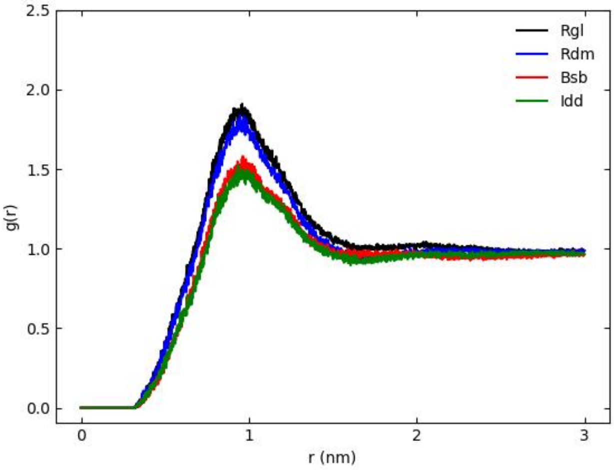

(b) cation-cation rdf

Figure 6.2: Radial distribution function of anion cloud or cation cloud at 500K trajectory

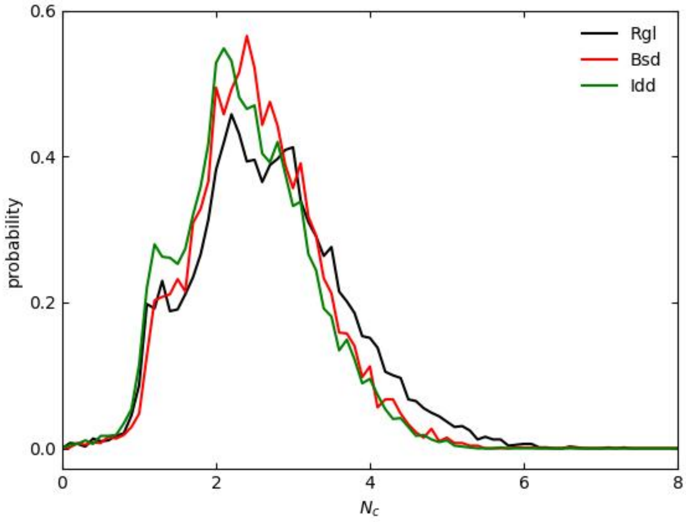

Figure 6.3: Probability distribution of coordination numbers at 500K trajectory

additional negative charges help reduce their potential energy. Consequently, ion aggregation is energetically favorable in the natural state. For free anions, due to their higher mobility, they naturally form higher coordination numbers compared to bonded anions, leading to a more uneven distribution of ions.

In a perfectly homogeneous distribution, the number density of anions is approximately $1024 \div (20 \cdot 10 \cdot 20) = 0.256$. Thus, the average number of anions within a spherical region of 1 nm radius is roughly $0.256 \cdot \frac{4\pi}{3}(1 \cdot 1 \cdot 1) = 1.07$. However, the data show that at 500 K, both free and bonded anions have average values slightly above 2, with Rgl at 2.69, Bsb at 2.53, and Idd at 2.40. This deviation in bonded anion systems is due to the fact that bonded anions are designed as dimers and the high mobility of TPS molecules, which allows them to migrate toward regions with higher anion aggregation. In contrast, in the free anion system, the deviation in the averaged N_c value is even more pronounced than in the bonded-anion system. This indicates that free anions experience significant aggregation at high temperatures, leading to a more uneven distribution of the system's acid sites. Additionally, Figure 6-3 shows that there are almost no TPS molecules with a coordination number of 0 in the system. This indicates that the electric field strength in simulation is sufficiently high to replicate the close ion pair relationships found in the photoresist.

Since the wafer undergoes post-exposure bake during the exposure process, which gradually increases the system temperature, it is important to understand how the degree of ion aggregation changes at various temperatures. Therefore, the average coordination number and standard deviation at different temperatures are plotted in Figure 6-4. We can observe that the effect of temperature on the coordination number is relatively minor compared to the standard deviation within the system. This indicates that the distribution of N_c is broad, with most TPS molecules having 1 to 3 coordinated anions. It's important to note that the coordination environment significantly impacts the efficiency of liberating anions from the positive charge of TPS, which is crucial for the generation of acids in PAGs. As the system temperature gradually increases, the coordination number between ions and anions also becomes higher, demonstrating a tendency for greater aggregation with heating. Phase separation induced by high temperatures is rarely observed in small molecule systems because, in most cases, the entropy of mixing is positive. However, in systems with a large amount of polymer, the significant difference in mobility between the polymers and small molecules—especially at high temperatures where the disparity is more pronounced—can lead to mixing that restricts the mobility of the small molecules, thereby reducing the system's entropy. The lowest temperature at which this phenomenon occurs is known as the lower critical solution temperature (LCST).

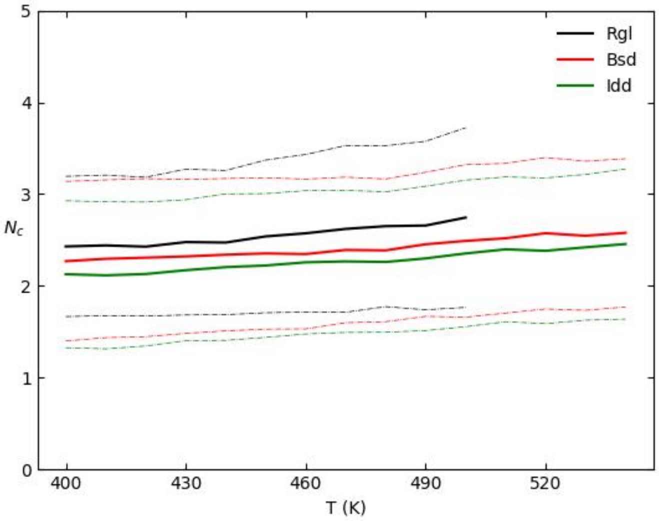

Figure 6.4: The averaged ccordination number at various temperature

6.2 Local Density Distribution of PAG

In the previous section, we observed that PAG coordination shows a denser and more pronounced trend in the free anion system compared to the bonded anion system. This section will show how this enhanced coordination affects the degree of non-uniformity within the system.

6.2.1 Phase separation due to high temperature

Slightly increased coordination number was observed at higher temperature. In order to reveal whether this increase in the PAG coordination number is accompanied by ion aggregation phenomena, the RDF of anion-anion and cation-cation pairs at different temperatures are analyzed to assess the extent of ion aggregation. As shown in Figure 6-5, the peak area at 500K is significantly higher than at 450K, while the peak area at 450K shows only a slight increase compared to the peak area at 400K. The peak area in RDF is proportional to the average of coordination number. Moreover, the increase at 450K

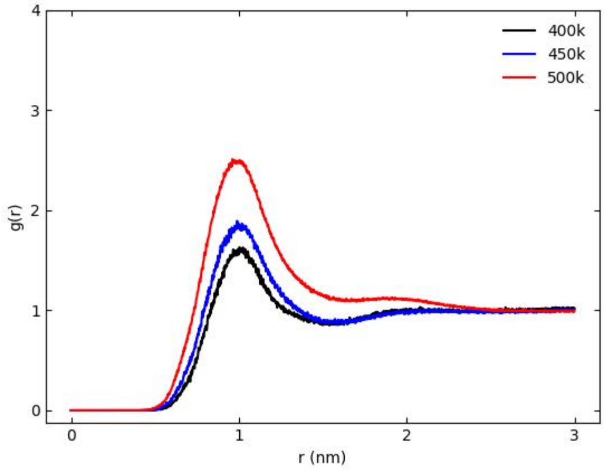

(a) anion-anion rdf

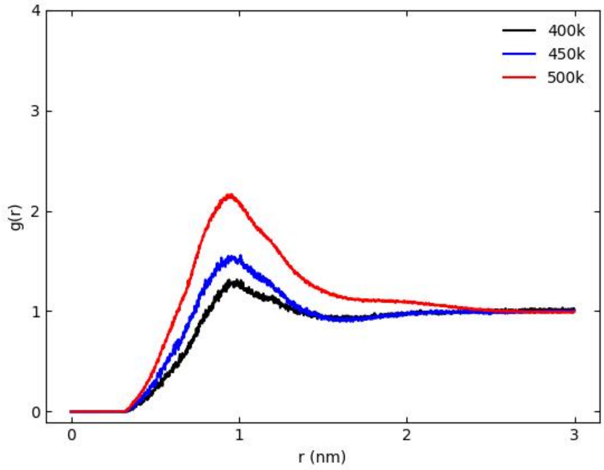

(b) cation-cation rdf

Figure 6.5: Radial distribution fucntion of anion cloud or cation cloud at various temperature

is observed only around 1 nm, whereas the increase at 500K extends to approximately 2 nm. This indicates that ion aggregation notably increases with rising temperature, and the coordination range seems to evolves from small ion clouds to the formation of an ionic phase.

Slight phase separation induced by high temperatures was inferred from the trend in the coordination number as heating progressed. However, to further verify this phenomenon, we need to analyze the system on a larger scale. Therefore, single linkage clustering was performed on the PAG and anions. The clusters are computed using critical distances of 0.5 nm, 0.8 nm, and 1 nm, which correspond to the first primary peak, the second primary peak, and the secondary peak of the RDF between TPS and anions, respectively. For each critical distance, the maximum number of groups was recorded in the system at various temperatures and plotted in Figure 6-6. We can observe that when the critical distance is 1 nm, the maximum group number increases with temperature. Therefore, 1 nm was chosen as the critical distance for identifying clusters, as this distance encompasses the majority of structural features observed in the cation-anion RDF. It is concluded that the largest ion cluster in the free anion systems exhibit a more pronounced growth with temperature. This trend is consistent with the previously noted increase in the averaged coordination number, both of which reflect the enhanced ion aggregation with temperature in these systems.

Subsequently, I also calculated the cation clusters composed solely of TPS sulfur and the anion clusters composed of anion sulfur, based on the 1 nm critical distance. The relationship between the group members of the largest cluster and temperature is illustrated in Figure 6-7. It is evident that at low temperatures, the sizes of the largest ion clusters across the four systems are initially similar. However, as the temperature increases, a noticeable trend of gradual aggregation is observed in the largest ion cluster within the free anion systems.

6.2.2 Ideal distribution and simulated distribution of anions

To examine the spatial uniformity of each system, the number density distribution of anions are analyzed for each system. The systems are divided into a total of 500 equally sized regions, each approximately 2 nm × 2 nm × 2 nm, and counted for the number of

doi:10.6342/NTU202404559

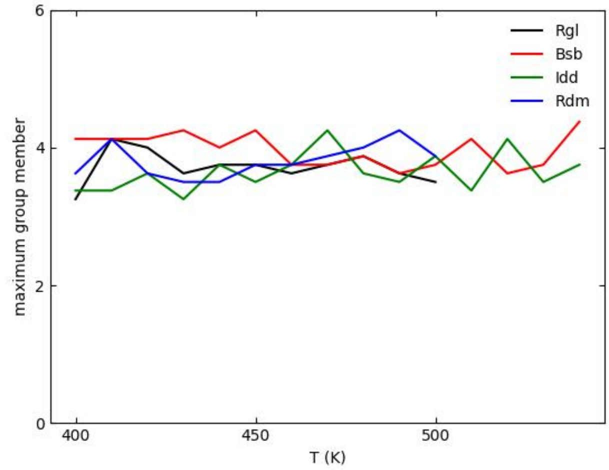

(a) ion cluster (0.5 nm)

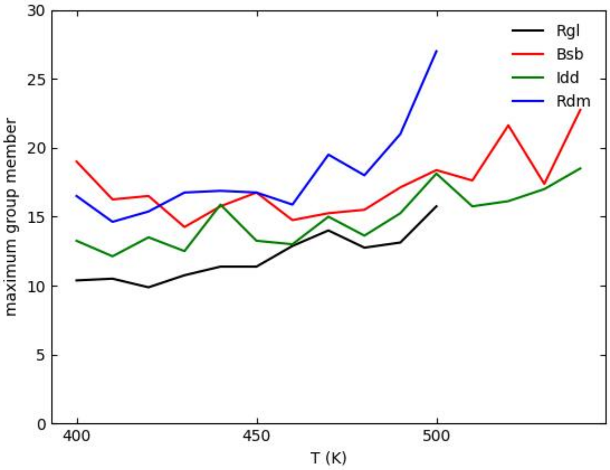

(b) ion cluster (0.8 nm)

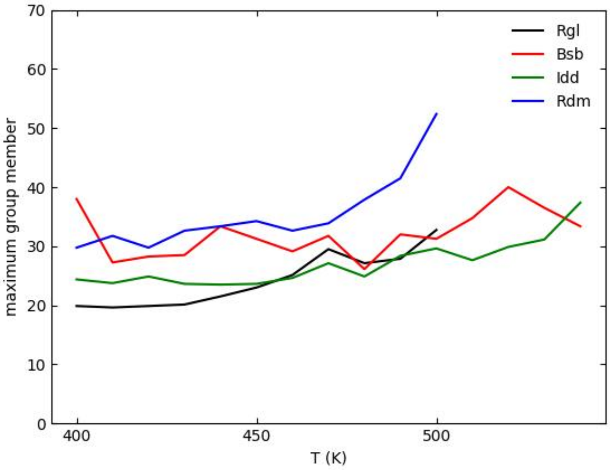

(c) ion cluster (1 nm)

Figure 6.6: Clustering at various level of critical distance

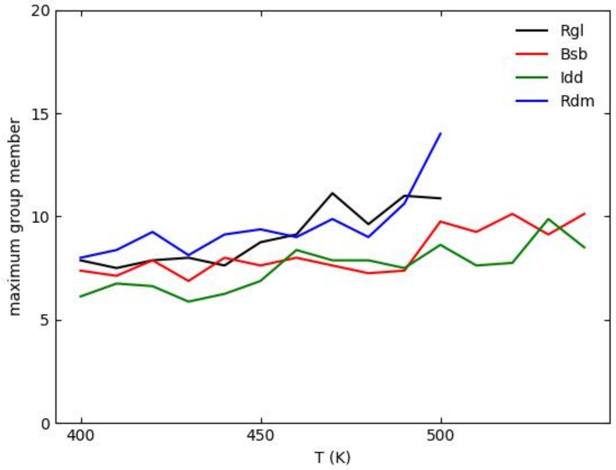

(a) anion cluster

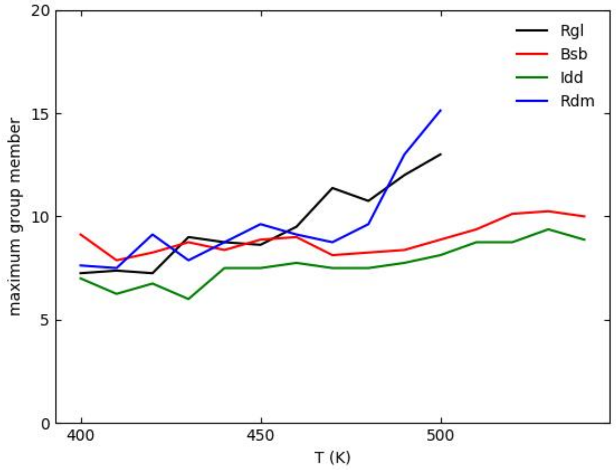

(b) cation cluster

Figure 6.7: Clustering of anions or cations

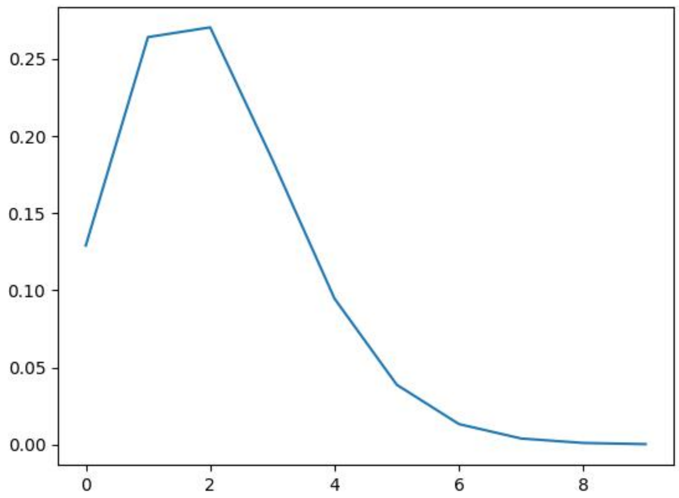

Figure 6.8: Poisson distribution of anion numbers in a box

anions in each box. Since the volume of the anion-bound polymer system is larger, using equally sized boxes compared to the free anion system would lead to an underestimation of the number of anions. Therefore, the actual sizes of the boxes varied among the different systems. The local number density in various regions are presented in Figure 6-9. Additionally, to establish a consistent comparison basis across the three systems, Poisson distribution is considered the ideal distribution of anion densities. The Poisson distribution is a probability distribution that describes the average rate of occurrence within a fixed interval of space for events occur independently. The formula for the Poisson distribution is given by:

$$P(x) = \frac{\lambda^x \exp(-\lambda)}{x!} \tag{6.1}$$

In the formula, x represents the number of anions observed in a given box, $P(x)$ denotes the probability of observing exactly x ions in that box, and λ is the expected number of ions in the box.

Ignoring the effects of all interactions, a completely random distribution would fol-

doi:10.6342/NTU202404559

low a Poisson distribution with a mean of 2.048 (Figure 6-8). The number density distributions of various systems are computed at different temperatures and compared with the Poisson distribution. However, Poisson distribution does not consider the electrical nature of anions. The behavior of anions is influenced by their electronic interactions, including repulsion between anions and attraction through packing with cations. These interactions lead to deviations from the Poisson distribution that reflects these physical constraints. At lower temperatures, anions were predominantly found in boxes containing two anions, with fewer occurrences of five or more anions aggregating in the same box, compared to the Poisson distribution. This deviation aligns with the effects of neglected anion volumes and interactions. Consequently, both the free-anion and bonded-anion systems closely followed this natural distribution at lower temperatures. However, at higher temperatures, ion aggregation intensified, causing deviations from the expected value of 2.048. We can observe an increase in the number of boxes with zero anions and a rise in boxes containing three or more anions. This deviation becomes particularly pronounced with increasing temperature, where significant increases in probability are observed, especially at $x = 0$ and $x = 5$. This shift indicates a stronger tendency for ions to cluster together, moving away from the Poisson distribution's prediction and reflecting increased ion aggregation within the system.

6.2.3 Characterization of distribution homogeneity

To assess the degree of ion aggregation, Moran's I is utilized to quantify the spatial connectivity of ions at multiple temperatures across three systems, including Rgl, Bsb and Idd. The temperature ranges from 400K to 500K for Rgl systems, and to 540K for Bsb and Idd systems. In the analysis, number of box (N) is 500, and the number of ions within

doi:10.6342/NTU202404559

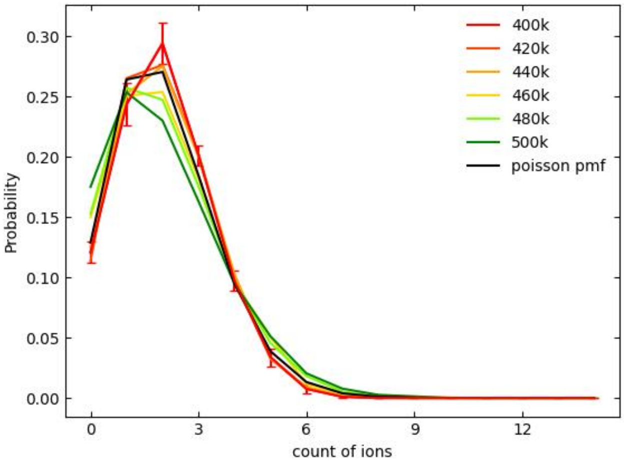

(a) Rgl

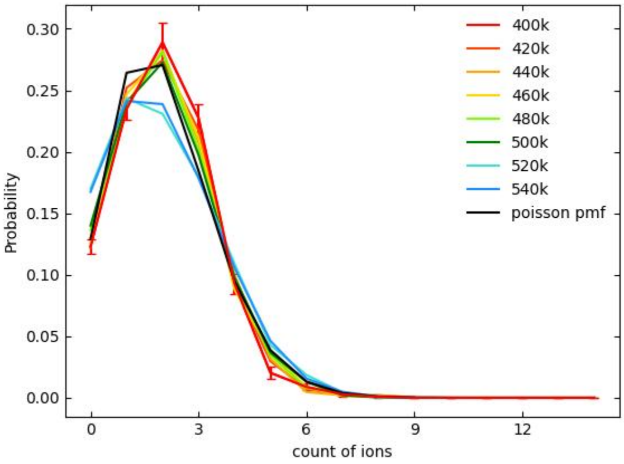

(b) Bsb

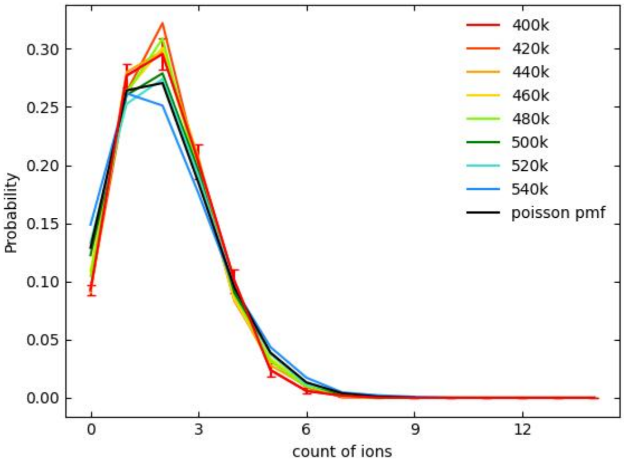

(c) Idd

Figure 6.9: Distribution of anion numbers in a box

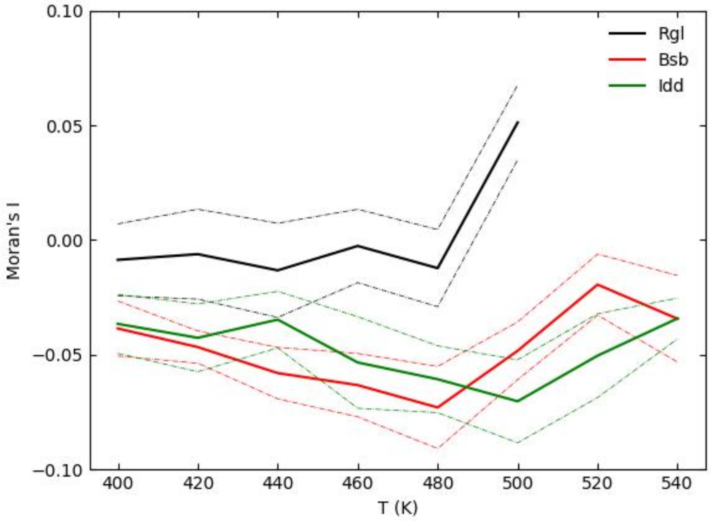

Figure 6.10: Moran's I of PR systems with various types of anions

each box ranges from 0 to 8, where the average number of ions is always 2.048. The calculated value are presented in Figure 6-10.

The values of Moran's I for each system and all temperatures were computed starting from the 10 ns mark of the trajectory, with calculations performed every 3 ns thereafter. The average values are indicated by a solid line, while the standard deviations are represented by a dotted line. At low temperatures, the free anion system (Rgl) and the bonded anion system (Bsb and Idd) exhibit similar Moran's I values, indicating comparable degrees of clustering. However, as the temperature increases, the free anion system tends to form larger clusters more readily, while the bonded anion system maintains a more consistent, moderate level of aggregation.

6.3 Polymer-PAG Interaction

In 2018, our lab have found that PAG may interact with the polymers and affect the chemical distribution of components in the photoresist. In previous studies, the cations tends to interact with acyl oxygens and anions tends to interact with phenols in 300K[32]. To compare these research findings, I investigate whether the ion clusters exhibit a preference for specific regions within the polymer matrix. As a result, the RDF of the ions with respect to the three distinct polymer units are analyzed using MD trajectories at 500 K. In this analysis, all ions were considered in detail, while each polymer unit was represented by a single oxygen atom. This approach minimizes directional bias in the ion analysis and ensures that the results are not influenced by the individual volumes of the polymer units. The RDF for the anions is shown in Figure 6-11, while the RDF for the cations is displayed in Figure 6-12.

In Figure 6-11, the RDF of anions relative to the polymer units are analyzed across the four systems. In the bonded-anion system, where anions are consistently located adjacent to unit C, their interaction is the most pronounced. However, in the free anion system, we observe results similar to those reported in previous studies, where anions exhibit a distinct interaction with unit A.[32] In the RDF, a peak is observed at approximately 0.5 nm, indicating a significant interaction at this distance. In contrast, the interactions between anions and other units are less pronounced. This is likely due to the interaction between the negative charge on the anion and the hydroxyl group present on the phenol. In the random copolymer system, due to the absence of distinct blocks within the system, all three types of units exhibit a certain degree of structure with the anions. It highlights that block copolymers significantly influence ion distribution.

The RDF of cations relative to the polymer units are analyzed across the four systems (Figure 6-12). In the free anion systems, TPS does not exhibit significant structural features with the polymer compared to the anions. However, in the bonded-anion systems, TPS shows a strong interaction with unit C, indicating that the position of TPS is primarily

doi:10.6342/NTU202404559

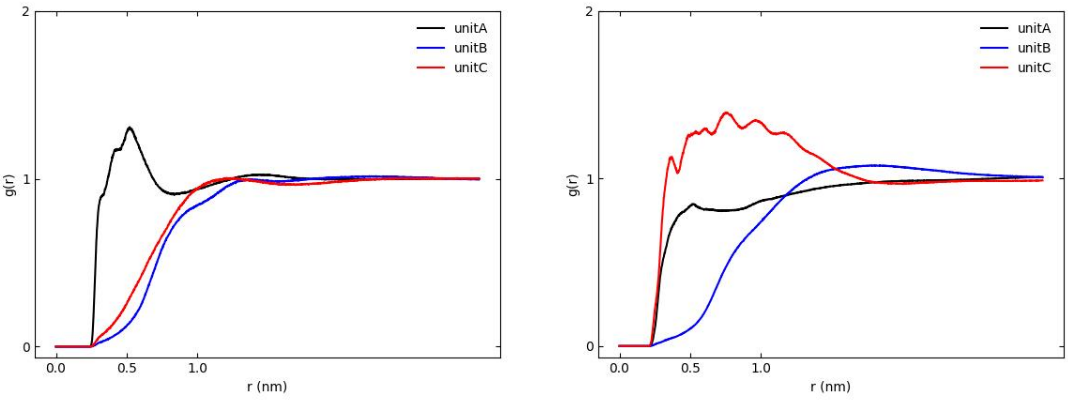

(a) Rgl (c) Bsb

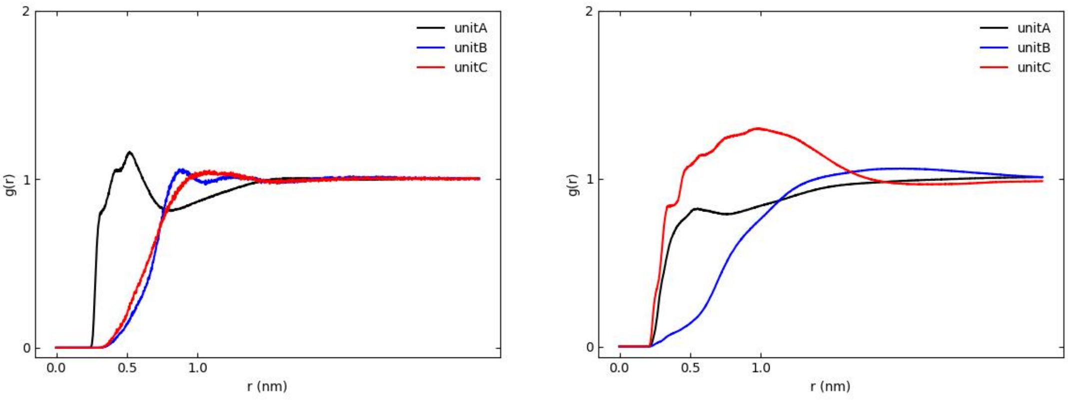

(b) Rdm (d) Idd

Figure 6.11: Radial distribution function from anion to three types of polymer unit

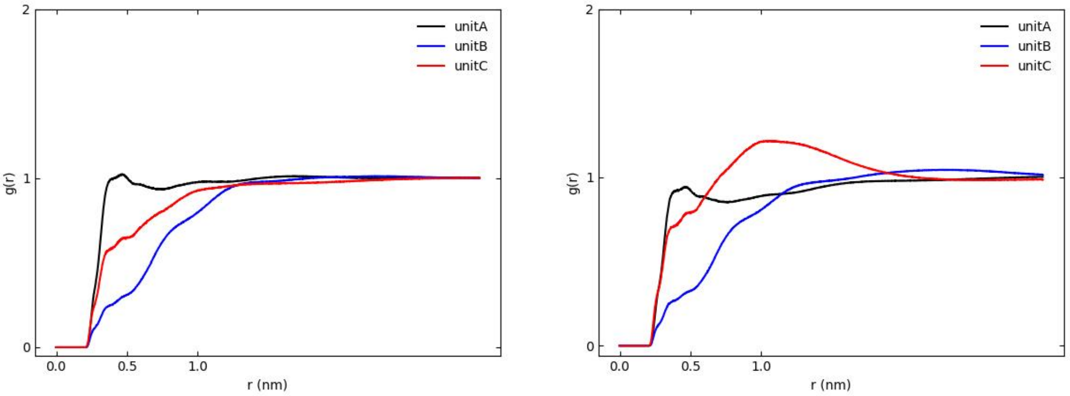

(a) Rgl

(c) Bsb

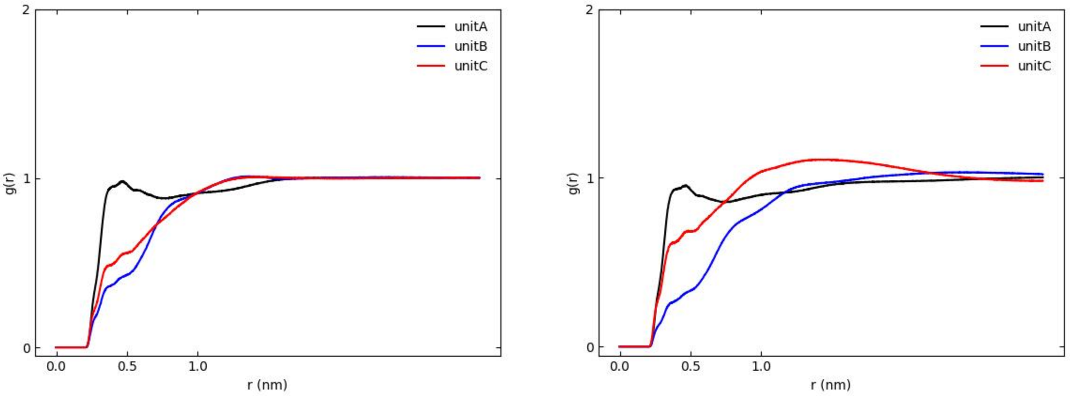

(b) Rdm

(d) Idd

Figure 6.12: Radial distribution function from TPS to three types of polymer unit influenced by the anions.

Their findings differ from previous research, likely due to temperature differences. Past studies prepared the matrix at 300K under standard pressure, while this thesis aims to observe the polymer matrix in the PEB state, simulating at 500K. At higher temperatures, the interaction between TPS and acyl oxygens becomes insignificant and disappears. This may also be due to the difficulty of ion and polymer mixing at elevated temperatures.

doi:10.6342/NTU202404559

Chapter 7 Mobility of Chemicals in CAR

In CAR lithography, anions with high mobility help reduce issues related to uneven light acid distribution caused by various factors, but they also blur the aerial image. These two effects are antagonistic when it comes to controlling LER, so it is necessary to continuously adjust the system structure during experiments to measure anion mobility. With MD simulation, we can observe how various conditions affect anion mobility, which can then help refine the experimental system structure to achieve reduced LER. In Chapter 6, we have observed that the system undergoes phase separation at higher temperatures. The difference in mobility between the polymers and PAGs may be a significant contributing factor. Therefore, this chapter will present the changes in mobility of both components with temperature. Also, it is important to investigate how polymer flexibility changes with temperature since this reflects the system's glass transition temperature (Tg) and affects the conditions of experimental temperature. In the CAR system, it is crucial to ensure that the temperature does not exceed Tg during the reaction, as it may lead to pattern distortion. Tg is considered a kinetic phenomenon, representing the temperature range over which the polymer transitions from a glassy state to a molten state. This phenomenon is often observed at a macroscopic level, which makes it challenging to measure with an

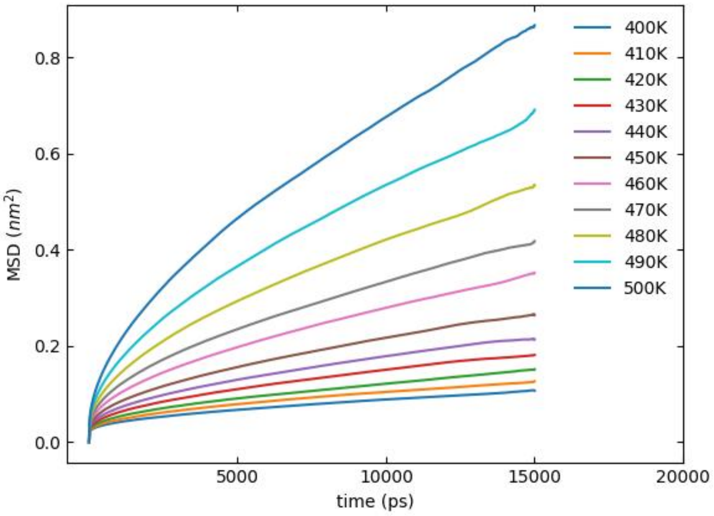

Figure 7.1: MSD of Rgl PR system

atomic model. Even experimentally, Tg can vary depending on the measurement method used.[33] Nevertheless, this temperature range is believed to result from the relaxation times of various structures and different chain motions. Therefore, we attempt to define the glass transition temperature of the simulation model based on polymer motion.

7.1 Diffusion of PAG

To quantify the mobility of PAG in the system, I measured the mean square displacement (MSD) of PAG atoms in MD trajectories at various temperatures to calculate the diffusion coefficients. The MD trajectories are each 25 ns in duration, with the initial 10 ns discarded as the equilibration period. Consequently, the reference time begins at 10 ns. Note that in Figure 7-1, the 25 ns trajectory is depicted as a 15 ns trajectory for clarity.

Diffusion coefficients are determined by fitting the slope to MSD versus time relationship across different temperatures, specifically using the data from 5 to 15 ns for all CAR systems, as illustrated in Figure 7-2. The diffusion coefficient serves as an indicator

doi:10.6342/NTU202404559

of mobility or flexibility, reflecting the rate at which the center of mass of an atom or molecule moves.

In the free anion system, anions exhibited higher diffusion coefficients compared to the bonded anion system. As shown in Figure 7-2, this is expected because, in the bonded anion system, one end of the anion is anchored to the polymer endpoint, which significantly reduces anion mobility. Interestingly, cations in the free anion system also display higher diffusion coefficients. I believe this is due to the influence of the anion’s position. In the free anion system, the cation and anion can move together more easily, whereas in the bonded anion system, the cation must overcome additional potential energy due to coordination with the anion to move. Evidence for this is that the reduction in the diffusion coefficient of cations in the bonded-anion system is not as pronounced as it is for anions. Therefore, if the distribution of bonded anions were more uniform, the diffusion of cations could be better preserved.

7.2 Flexibility of Polymer

Similarly, MSD can be used to measure polymer flexibility. All atoms in polymers that do not belong to PAG are collected, and their MSD is measured under the same conditions as for PAG. The overall diffusion coefficient is then calculated based on their MSD, as presented in Figure 7-3.

Similar to the trend observed with PAG, the polymer in the free anion system exhibits higher flexibility. At lower temperatures, the difference is not significant. However, as the temperature increases, the bonded anions restrict polymer movement, effectively reducing the polymer’ s entropy. This result confirms the hypothesis presented in Chapter 6: the

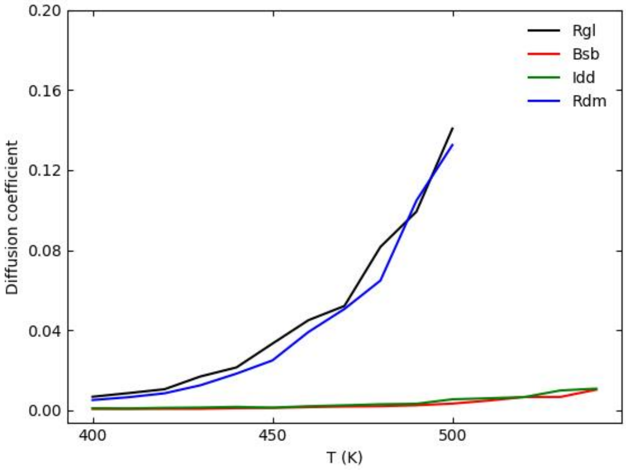

(a) anion msd

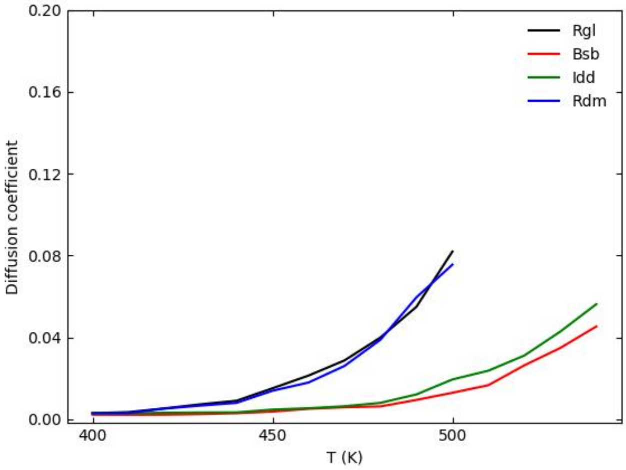

(b) cation msd

Figure 7.2: Diffusion coefficients of PAG at various temperature

doi:10.6342/NTU202404559

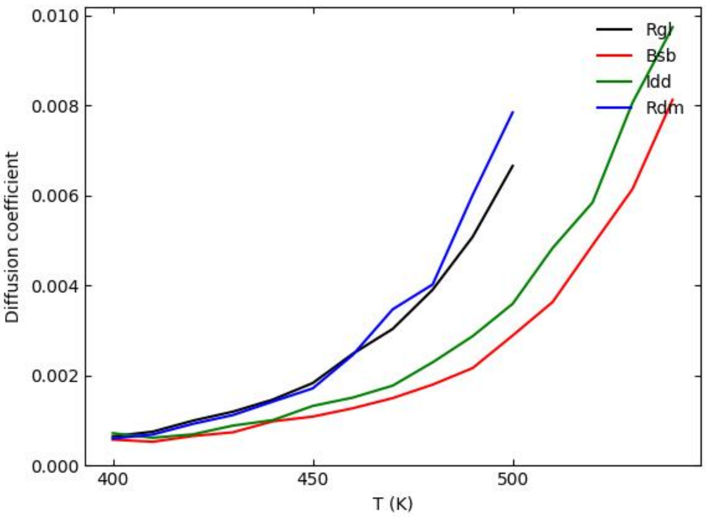

Figure 7.3: Diffusion coefficients of polymers at various temperature

mixing of PAG and polymer decreases the system's entropy, as both their mobilities are restricted in bonded-anion systems.

To gain deeper insights into the flexibility of polymers, the flexibility of each type of units were computed, whose diffusion coefficient are present in Figure 7-4 respectively. We can observe that the flexibility of unitB is slightly lower compared to other units, indicating that the steric hindrance introduced by unitB creates a more rigid backbone in these block copolymers. This rigidity in the midsection of the polymer plays a crucial role in increasing the persistence length of the block copolymers and enlarging the grain size of the polymer.

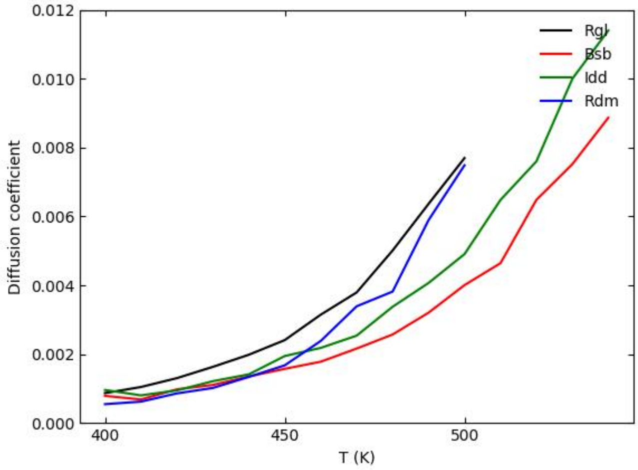

(a) unitA msd

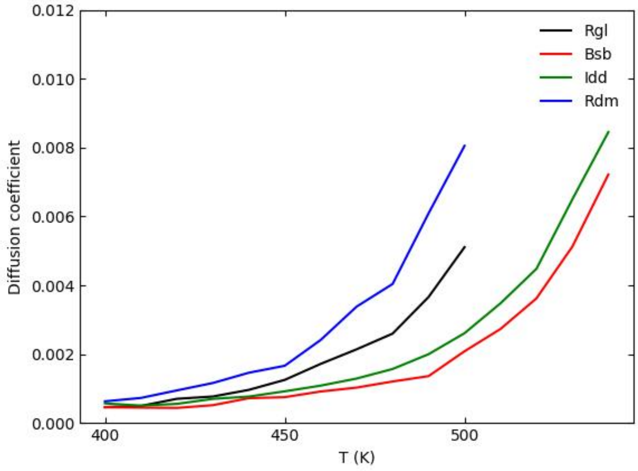

(b) unitB msd

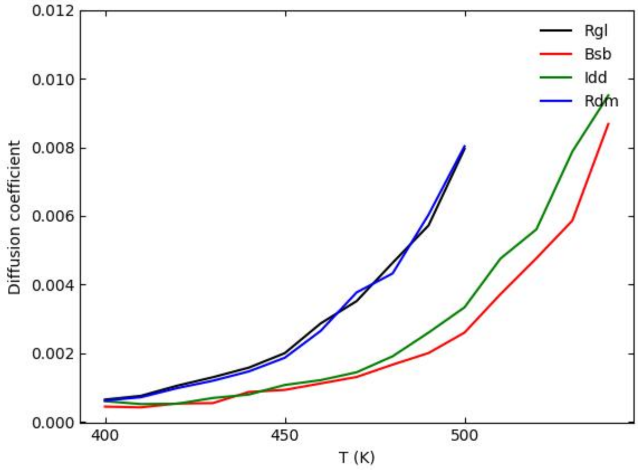

(c) unitC msd

Figure 7.4: Diffusion coefficients of three types of polymer units at various temperature

7.3 Glass Transition Temperature of CAR Polymers

In 1904, Einstein established a relationship between gas diffusion and temperature, commonly referred to as the Einstein relation, expressed as the following equation:

$$D = \mu k_B T \tag{7.1}$$

In this equation, D represents the diffusion coefficient of gas molecules, μ represents the gas mobility, measured as the ratio of the terminal drift velocity to an applied force, k_B is the Boltzmann constant, and T is the temperature. According to the Einstein relation, the diffusion coefficient of gas molecules is proportional to temperature, assuming the mobility of the molecules does not significantly change with temperature. However, because the structure of polymers is much more complex than that of gas molecules, the mobility of polymers can undergo dramatic changes over a specific temperature range. Consequently, the diffusion coefficient of polymers exhibits a highly non-linear behavior. The temperature range where this dramatic change in mobility occurs is referred to as the glass transition temperature (Tg) of the polymer. Traditionally, Tg is identified as the temperature at which mobility changes most sharply. In experiments, direct observation of polymer mobility is challenging, so various indirect indicators are used to determine Tg. However, these methods often yield different Tg values for the same polymer, depending on the measurement technique. In contrast, in MD simulations, we can directly observe polymer mobility without needing to mimic experimental procedures. To measure Tg in simulations, we can utilize the Einstein relation to calculate polymer mobility (μ) and thus define Tg. In the previous section, we plotted the diffusion coefficient against temperature. The polymer's mobility can be represented by the slope of this plot (Figure 7-5). The

doi:10.6342/NTU202404559

Table 7.1: Glass transition temperature of polymer

System name	polymer	unitA	unitB	unitC
Regular-sequenced polymer (Rgl)	467.7	462.8	471.8	467.5
Random-sequencedpolymer (Rdm)	469.8	469.8	470.1	469.0
Besylate-bonded polymer (Bsb)	500.5	483.7	506.6	504.7
Iodine-doped polymer (Idd)	498.7	492.7	503.8	497.9

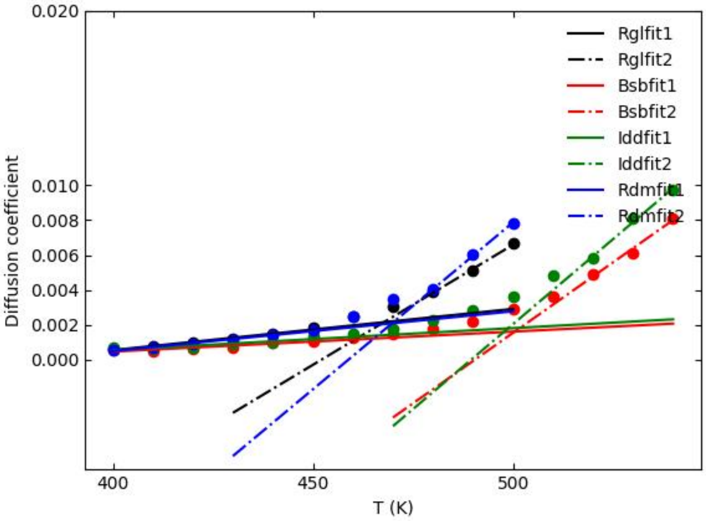

Figure 7.5: Determining the glass transition temperature of polymer

two slopes, corresponding to the low-temperature and high-temperature regions, represent the polymer's mobility before and after Tg[34]. The Tg is identified at the intersection of these two slopes. The slope in the lower temperature region is obtained from data in the 400K–450K range using the least-squares method. For the higher temperature region, the slope is derived from data in the 480K–500K range for the free anion systems, and in the 520K–540K range for the bonded-anion systems. The Tg values of the polymers in the four systems are presented in Table 7-1. Furthermore, each unit blocks on the same polymer may exhibit different Tg[35]. To further investigate the polymer mobility, the Tg of individual unit blocks within the polymer are also calculated (Figure 7-6).

Overall, the polymers in bonded-anion systems exhibit a higher Tg compared to those

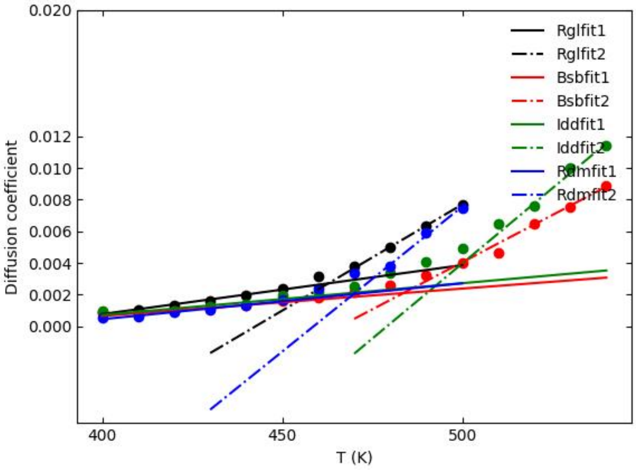

(a) Determining the glass transition temperature of unitA

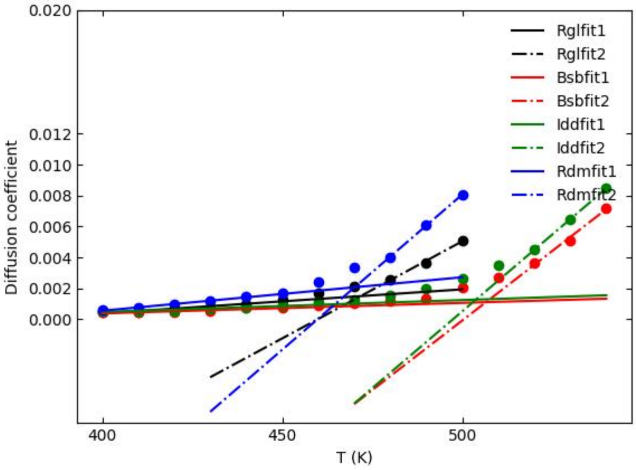

(b) Determining the glass transition temperature of unitB

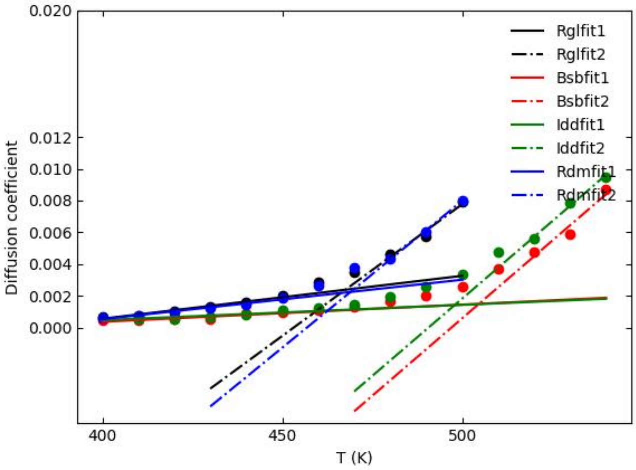

(c) Determining the glass transition temperature of unitC

Figure 7.6: Determining the glass transition temperature of three types of polymer unit

in free anion systems. It suggests that a more uniform ion distribution reduces the mobility of both the polymers and ions. Due to the increased contact area between the ions and the polymer, the highly mobile ions effectively hinder the movement of the polymer, thus reducing both mobility and entropy. In the previous chapter, this study also observed that the entropy of mixing decreases at high temperatures in this system, which is consistent with these findings.

Regarding polymer permutation, the different blocks in block copolymers exhibit varying Tg values, largely due to the particularly bulky nature of unit B. In contrast, this issue is much less pronounced in random copolymers. It indicates that as long as bulky polymer units like unit B are prevented from direct interaction, their inherent high rigidity can remain hidden.

doi:10.6342/NTU202404559

Chapter 8　Conclusion

This study has provided valuable insights into the behavior of CARs through MD simulations, focusing on the structural and dynamic properties of polymers and ions. One of the key findings is the influence of steric effects on polymer packing. The simulation results demonstrate that the stacking of polymer units with higher steric hindrance reduce the overall flexibility of the polymer chains. As a result, these more rigid polymers tend to elongate, increasing the overall length and impacting the structural arrangement of the polymer matrix.

Furthermore, the incorporation of bonded anions into the polymer matrix was shown to reduce ion aggregation, not only for anions but also for cations. This reduction in ion aggregation aligns with experimental findings reported in previous studies, reinforcing the hypothesis that bonded anions create a more homogeneous ionic distribution within the polymer matrix. By averaging local ion concentrations, bonded anions improve the overall pattern fidelity and reduce defects caused by uneven ion distribution during the development process.

Another critical observation from this study is the enhancement of ion aggregation upon heating. As the temperature increases, the mobility difference between the polymer and the ions becomes more pronounced. The polymer matrix, being more rigid at higher temperatures, restricts the movement of ions, leading to greater ion clustering. This phenomenon, driven by the disparity in mobility between the polymer chains and the ions, could lead to performance degradation in CAR systems, particularly at elevated processing temperatures.

In conclusion, the packing characteristics of polymers, the role of bonded anions in minimizing ion aggregation, and the temperature-dependent behavior of ions are critical factors that must be considered in the development of high-performance resists for advanced lithographic processes. These findings not only provide a deeper understanding of the underlying mechanisms but also offer practical guidance for optimizing resist formulations in future semiconductor manufacturing.

References

[1] C. Grant Willson, Ralph R. Dammel, and Arnost Reiser. Photoresist materials: a historical perspective. In Advances in Resist Technology and Processing XIV, volume 3050, pages 38–51, 1997.

[2] Muhammad Hassaan, Umama Saleem, Akash Singh, Abrar Jawad Haque, and Kaiying Wang. Recent advances in positive photoresists: Mechanisms and fabrication. Materials, 17:2552, 2024.

[3] Theodore Manouras and Panagiotis Argitis. High sensitivity resists for euv lithography: A review of material design strategies and performance results. Nanomaterials, 10(8):1593, 2020.

[4] Jinwon Park, Jaehong Lee, Seongsoo Han, Hyun-Ro Lee, and Siyoung Q. Choi. Removal analysis of residual photoresist particles based on surface topography affected by exposure times of ultraviolet and developer solution. Langmuir, 38(51):16134–16143, 2022.

[5] Muyoung Kim, Junghwan Moon, Joonmyung Choi, Sungwoo Park, Byunghoon Lee, and Maenghyo Cho. Multiscale simulation approach on sub-10 nm extreme ultraviolet photoresist patterning: Insights from nanoscale heterogeneity of polymer. Macromolecules, 51(17):6922–6935, 2018.

[6] Mingxing Wang, Cheng-Tsung Lee, Clifford L. Henderson, Wang Yueh, Jeanette M. Roberts, and Kenneth E. Gonsalves. Synthesis and properties of new anionic photoacid generators bound polymer resists for e-beam and EUV lithography. In Advances in Resist Materials and Processing Technology XXV, volume 6923, page 692312, 2008.

[7] Florian Kaefer, Zoey Meng, Rachel Segalman, and Christopher K. Ober. Controlled sequence photoresists from polypeptoids. Journal of Photopolymer Science and Technology, 35(1):29–33, 2022.

[8] X. Zoey Meng, Florian H. Käfer, Gregory M. Wallraff, Christopher K. Ober, and Rachel A. Segalman. Controlled sequence peptoids as photoresist platforms for high-resolution DUV/EUV photoresists. In International Conference on Extreme Ultraviolet Lithography 2022, volume 12292, page 122920Q, 2022.

[9] Cameron P. Adams, Xiangxi Meng, Florian H. Kaefer, Chenyun Yuan, Christopher K. Ober, and Rachel A. Segalman. Sequence-defined polypeptoids as DUV and EUV chemically amplified resists. In International Conference on Extreme Ultraviolet Lithography 2023, volume PC12750, page PC127500J, 2023.

[10] Muyoung Kim, Junghwan Moon, Sungwoo Park, and Maenghyo Cho. Selective dissolution resistance control of euv photoresist using multiscale simulation: Rational design of hybrid system. Macromolecules, 53(12):4748–4763, 2020.

[11] Lei Guo and Erik Luijten. Reversible gel formation of triblock copolymers studied by molecular dynamics simulation. Journal of Polymer Science Part B: Polymer Physics, 43(8):959–969, 2005.

[12] J. M. Haile. Molecular Dynamics Simulation: Elementary Methods. Wiley, New York, 1992.

[13] H. J. C. Berendsen, J. P. M. Postma, W. F. van Gunsteren, A. DiNola, and J. R. Haak. Molecular dynamics with coupling to an external bath. The Journal of Chemical Physics, 81(8):3684–3690, 1984.

[14] Jean-Paul Ryckaert, Giovanni Ciccotti, and Herman Berendsen. Numerical-integration of cartesian equations of motion of a system with constraints -molecular-dynamics of n-alkanes. Journal of Computational Physics, 23:327–341, 1977.

[15] Michael Rubinstein and Ralph H. Colby. Polymer physics, 2003.

[16] Rodolfo G. Pereyra and Marcelo A. Carignano. Molecular dynamics study of polymeric chemical gels: Effect of persistence length and crosslinker density. Journal of Polymer Science Part B: Polymer Physics, 57(19):1343–1350, 2019.

[17] Loes M. J. Kroon-Batenburg, Peter H. Kruiskamp, Johannes F. G. Vliegenthart, and Jan Kroon. Estimation of the persistence length of polymers by md simulations on small fragments in solution. application to cellulose. The Journal of Physical Chemistry B, 101(42):8454–8459, 1997.

[18] Handan Arkın and Wolfhard Janke. Gyration tensor based analysis of the shapes of polymer chains in an attractive spherical cage. The Journal of Chemical Physics, 138(5):54904, 2013.

[19] Meilin Li and Stefan Adams. Molecular dynamics simulations of cation-controlled aggregation in fluorene-triarylamine copolymers. Journal of Polymer Science Part B: Polymer Physics, 54(10):965–974, 2016.

[20] Matteo Paloni, Rémy Bailly, Luca Ciandrini, and Alessandro Barducci. Unraveling molecular interactions in liquid–liquid phase separation of disordered proteins by atomistic simulations. The Journal of Physical Chemistry B, 124(41):9009–9016, 2020.

[21] Junmei Wang, Romain M. Wolf, James W. Caldwell, Peter A. Kollman, and David A. Case. Development and testing of a general amber force field. Journal of Computational Chemistry, 25(9):1157–1174, 2004.

[22] Wendy D. Cornell, Piotr Cieplak, Christopher I. Bayly, Ian R. Gould, Kenneth M. Merz, David M. Ferguson, David C. Spellmeyer, Thomas Fox, James W. Caldwell, and Peter A. Kollman. A second generation force field for the simulation of proteins, nucleic acids, and organic molecules. Journal of the American Chemical Society, 117(19):5179–5197, 1995.

[23] Samira Anker, David McKechnie, Paul Mulheran, Jan Sefcik, and Karen Johnston. Assessment of gaff and opls force fields for urea: Crystal and aqueous solution properties. Crystal Growth & Design, 24(1):143–158, 2024.

[24] Rahul Bhowmik, Sangwook Sihn, Vikas Varshney, Ajit K. Roy, and Jonathan P. Vernon. Calculation of specific heat of polymers using molecular dynamics simulations. Polymer, 167:176–181, 2019.

[25] Christopher I. Bayly, Piotr Cieplak, Wendy Cornell, and Peter A. Kollman. A well-behaved electrostatic potential based method using charge restraints for deriving atomic charges: the resp model. The Journal of Physical Chemistry, 97(40):10269–10280, 1993.

doi:10.6342/NTU202404559

[26] Oscar Parreño, Pablo Miguel Ramos, Nikos Ch. Karayiannis, and Manuel Laso. Self-avoiding random walks as a model to study athermal linear polymers under extreme plate confinement. Polymers, 12(4):2073–4360, 2020.

[27] Franco Ormeño and Ignacio J. General. Convergence and equilibrium in molecular dynamics simulations. Communications Chemistry, 7(1):26, 2024.

[28] George P. Patsis, Vassilios Constantoudis, and Evangelos Gogolides. Effects of photoresist polymer molecular weight on line-edge roughness and its metrology probed with monte carlo simulations. Microelectronic Engineering, 75:297–308, 2004.

[29] Juhae Park, Sung-Gyu Lee, Yannick Vesters, Joren Severi, Myungwoong Kim, Danilo De Simone, Hye-Keun Oh, and Su-Mi Hur. Molecular modeling of euv photoresist revealing the effect of chain conformation on line-edge roughness formation. Polymers, 11(12):1923, 2019.

[30] Pedro J. Rodríguez-Cantó, Ulrich Nickel, and Rafael Abargues. Understanding acid reaction and diffusion in chemically amplified photoresists: An approach at the molecular level. The Journal of Physical Chemistry C, 115(42):20367–20374, 2011.

[31] Jin Bong Shin, Hyun Sang Joo, Seung Duk Cho, Hyun Soon Lim, Jin Ho Kim, Seung Jae Lee, Dae Hyeon Shin, JoonHee Han, and Dong Chul Seo. Study of acid diffusion of anionic or cationic polymer bound PAG. In Extreme Ultraviolet (EUV) Lithography II, volume 7969, page 79692N, 2011.

[32] Ping-Jui Wu, Yu-Fu Wang, Wei-Chi Chen, Chien-Wei Wang, Joy Cheng, Vencent Chang, Ching-Yu Chang, John Lin, and Yuan-Chung Cheng. Nanoscale inhomogeneity and photoacid generation dynamics in extreme ultraviolet resist materials.

In Advances in Patterning Materials and Processes XXXV, volume 10586, page 105861O, 2018.

[33] Jolanta Tomaszewska, Tomasz Sterzyński, Aneta Woźniak-Braszak, and Michał Banaszak. Review of recent developments of glass transition in pvc nanocomposites. Polymers, 13(24):4336, 2021.

[34] Anshuman Cherala and S. V. Sreenivasan. Molecular dynamics modeling framework for overcoming nanoshape retention limits of imprint lithography. Microsystems & Nanoengineering, 4(1):3, 2018.

[35] Min Zhang, Zhiwei Cui, and Lynda Catherine Brinson. Mechanical properties of hard–soft block copolymers calculated from coarse-grained molecular dynamics models. Journal of Polymer Science Part B: Polymer Physics, 56(23):1552–1566, 2018.